NASA Contractor Report 3009

Reduction of Computer Usage Costs in Predicting Unsteady Aerodynamic Loadings Caused by Control Surface Motions - Analysis and Results

W. S. Rowe, J. D. Sebastian,
and J. R. Petrarca

CONTRACT NAS1-14122
MARCH 1979

NASA

NASA Contractor Report 3009

Reduction of Computer Usage Costs in Predicting Unsteady Aerodynamic Loadings Caused by Control Surface Motions - Analysis and Results

W. S. Rowe, J. D. Sebastian,
and J. R. Petrarca
Boeing Commercial Airplane Company
Seattle, Washington

Prepared for
Langley Research Center
under Contract NAS1-14122

NASA
National Aeronautics
and Space Administration

Scientific and Technical
Information Office

1979

CONTENTS

SUMMARY

Results of theoretical and numerical investigations conducted to develop economical computing procedures have been applied to an existing computer program (see NASA CR-2543) that predicts unsteady aerodynamic loadings caused by leading and trailing edge control surface motions in subsonic compressible flow. Large reductions in computing costs are achieved by removing the spanwise singularity of the downwash integrand and evaluating its effect separately in closed form. Additional reductions are obtained by modifying the incremental pressure term that accounts for downwash singularities at control surface edges. Accuracy of theoretical predictions of unsteady loading at high reduced frequencies is increased by applying new pressure expressions that exactly satisfy the high frequency boundary conditions of an oscillating control surface. Comparative computer results indicate that the revised procedures provide more accurate predictions of unsteady loadings as well as providing reductions of 50 to 80 percent in computer usage costs.

INTRODUCTION

Theoretical and numerical investigations have been conducted to identify a means of reducing computer usage costs for application of the subsonic kernel function and downwash collocation process described in NASA CR-2543 for predicting unsteady aerodynamic loadings caused by leading and trailing edge control surface motions in subsonic compressible flow. It was determined that the program provided accurate predictions of unsteady loadings for the sample cases described in NASA CR-2543. However, computer usage costs severely limited its usefulness for general application in engineering analysis.

The computer program of NASA CR-2543 was developed with accuracy and ease of usage as primary requirements. The numerical approach that was employed provided the most accurate evaluation of the downwash discontinuity around the edges of the control surfaces and did not restrict the user in locating downwash stations in the near vicinity of the control surface edges.

The method employed for downwash evaluation in the vicinity of the control surface edges was to integrate the singularity of the spanwise integrand by numerical quadrature. Although this technique provides excellent downwash evaluations, it was found to be very costly, in that 40% of the downwash calculation time was involved in evaluating this small portion of the spanwise integrand that encloses the downwash station.

The present report describes an alternative method used to evaluate the singularity in the spanwise integrand. Use of this alternative method will introduce discontinuities in the calculated downwashes along the hinge line of the control surface. However, the region where the approximate downwashes differ from the correct values is restricted to a very small region near the hinge line. This should not cause any user apprehension concerning the validity of the solutions, provided that downwash collocation stations are not placed within the restricted regions.

Other techniques employed to reduce the computer usage costs consist of: 1) limiting the extent to which the control surface pressure terms are distributed over the planform, 2) reformulating a new integration algorithm to minimize the number of integration stations on the surface, and 3) reconstructing new pressure modification functions to reduce the waviness in residual downwashes.

The present work represents an extension of the analytical methods developed in reference 1 to provide a capability for predicting unsteady aerodynamic loadings caused by control surface motions that are both accurate and economical to use. The computer program is described in NASA CR-145354.

ABBREVIATIONS AND SYMBOLS

All quantities are dimensionless except as noted.

b	Length	Local semichord
b_0	Length	Reference length
c		Local chord length nondimensional with respect to b_0
E_1		Chordwise pressure modification function
$f(\eta)$		Spanwise distribution function of lifting pressure
$g(\xi, \eta)$		Chordwise distribution function of lifting pressure
i		$\sqrt{-1}$
$K(x, \xi, y, \eta)$		Kernel function
k		Reduced frequency $= \frac{\omega b_0}{V}$
M		Mach number of free stream
P_ℓ	Force/area	Perturbation pressure on lower surface
P_u	Force/area	Perturbation pressure on upper surface
ΔP	Force/area	Pressure difference, $P_\ell - P_u$ (positive upward)
ΔP_j	(Force/area)/unit q_j	Surface pressure difference in mode j
q_j		Generalized coordinate amplitude for mode j
R		$\sqrt{x_0^2 + \beta^2 y_0^2}$
s		Nondimensional semispan, S/b_0
t		Time
V	Length/time	Free stream velocity
$\frac{w}{V}$		Kinematic angle of attack or nondimensional normalwash
$\overline{W}$		$\frac{w}{V}$
$\overline{w}_j$		$w_j/q_j e^{i\omega t}$
x, y, z		Cartesian coordinates, nondimensional with respect to ℓ
x_ℓ		x coordinate of the leading edge
x_t		x coordinate of the trailing edge
x_0		$x - \xi$

x_{cs}		x coordinate of hinge line at side edge of control surface
$x_{\ell s}$		x coordinate of planform leading edge at side of control surface
y_0		y – n
y_s		y coordinate of control surface side edge
Z_{cs}		Surface deflection
β		$\sqrt{1 - M^2}$
β_h		$\sqrt{\beta^2 + \tan^2 \Lambda_c}$
β_ℓ		$\sqrt{\beta^2 + \tan^2 \Lambda_\ell}$
ΔC_p		Lifting pressure coefficient $(P_\ell - P_u)/(\frac{1}{2}\sigma V^2)$
Λ_h	Radian	Sweep angle of the control surface hinge line, positive swept back
Λ_ℓ	Radian	Sweep angle of leading edge, positive swept back on right-hand side
ξ_c		ξ coordinate of hinge line at span station η
ξ, η, ζ		Dummy variables for (x, y, z)
$\Theta_H(\eta)$	Radian	Rotation angle of control surface hinge line at (η), measured in the plane perpendicular to the y-axis and positive trailing edge down
ρ	Mass/length^3	Density of the fluid
τ	Time	Nondimensional time
ω	1/time	Circular frequency of oscillation

ANALYTICAL AND NUMERICAL PROCEDURES

AREAS OF INVESTIGATION

This report describes the procedures used to reduce computer usage costs involved in calculating unsteady aerodynamic loadings caused by control surface motions in subsonic flow. The procedures are applicable to planform configurations having full span or multiple partial span control surfaces with arbitrary spanwise location.

The analysis coordinate system is defined in figure 1 for a typical leading edge and/or trailing edge control surface configuration.

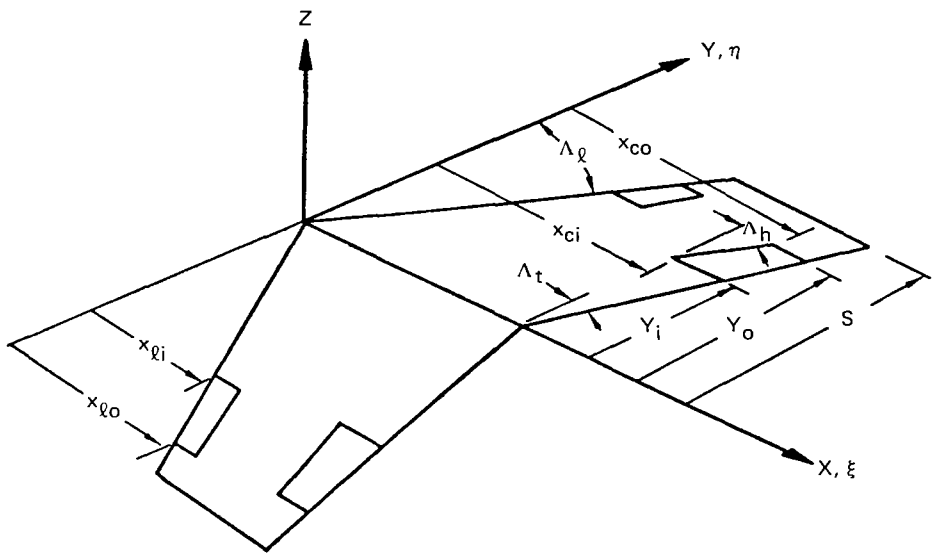

Figure 1.—Analysis Coordinate System

Analytical and numerical investigations have been conducted to evaluate the computational efficiency of the procedures used in the computer program described in NASA CR-2543.

Various areas of investigation that have led to changes in the structure of the original program are as follows:

1) Revison of the spanwise integration procedure for downwash calculation. The spanwise integrand contains a logarithmic singularity at the downwash station. It has been determined that the method formerly used for evaluation of the singular term required a very large portion of the overall computation time.

   Computational procedures have been revised so that the singular term is integrated separately, outside of the numerical quadrature process.

   Use of this alternate procedure will impose some restrictions on the placement of collocation stations in the near vicinity of the hinge line. However, it appears that this limitation will not severely hamper user applications. Accurate predictions of unsteady loadings may be obtained, provided the downwash collocation stations are not placed within the restricted regions.

2) Reductions in computer usage are achieved by revising the distribution of lifting pressures due to downwash discontinuities. In the original formulation, the pressure terms that were developed to satisfy the control surface boundary conditions were extended over the entire lifting surface, regardless of the magnitude of the pressures at large distances from the control surfaces. Pressures developed for motions of a control surface on the right-hand wing were extended to the left-hand wing and rolled off to zero to satisfy the boundary condition at the left-hand wingtip.

   The discontinuity related pressures have been found to be very small at moderate distances from the control surfaces. Consequently, the spanwise loading distributions have been modified by deleting the small loadings that do not contribute to solution accuracy.

3) Further reductions in usage costs are achieved by developing a suitable algorithm to minimize the number of integration stations necessary to provide downwash calculations within specified accuracy limits.

   Stringent requirements are imposed on the integration algorithm so that any large variations of the spanwise integrand are accurately accounted for in the analysis of planforms with arbitrary aspect ratio and taper ratio.

4) Cost reductions are also achieved by reducing the waviness of the residual downwashes so that only a small number of collocation stations are required to obtain accurate predictions of unsteady loadings for small span control surface configurations. Numerical investigations have indicated that accurate loading predictions require an increasing number of collocation stations to be distributed over the lifting surface in the chordwise direction as the chordwise length of the control surface tends to zero. Program modifications have been made to allow cost effective analyses of configurations having extremely small control surface chord lengths.

5) New pressure expressions that exactly satisfy the boundary conditions on a control surface oscillating at high frequency in high Mach number flow conditions have been developed and incorporated within the program. Derivation of new pressure expressions that are not frequency limited are presented in Appendix A and Appendix B.

Each of the above described items of interest is discussed in detail in the following sections.

MODIFICATION OF THE SPANWISE INTEGRATION TECHNIQUE

The downwash integral equation formulated within NASA CR-2543 is given as follows:

$$\pi\left(\frac{w}{V}\right) = \int_{-s}^{s} \sqrt{s^2-\eta^2}\, f(\eta) \left\{ \int_{x_\ell}^{x_t} g(\xi,\eta)\left[\underset{\text{singular}}{K(x,\xi,y,\eta)} + \underset{\text{non-sing.}}{K(x,\xi,y,\eta)}\right] d\xi \right.$$

$$\left. + \frac{2}{(y-\eta)^2}\, f(y) \int_{x_\ell}^{x} g(\xi,y)\exp(-ik(x-\xi))\, d\xi - \frac{G'(x,y,y)}{(y-\eta)} \right\} d\eta$$

$$+ \pi \left\{ 2\, f(y) \int_{x_\ell}^{x} g(\xi,y)\exp(-ik(x-\xi))\, d\xi + yG'(x,y,y) \right\} \qquad (1)$$

where

$f(\eta)$	is the spanwise variation of the pressure function
$g(\xi,\eta)$	is the chordwise variation of the pressure function
$K(x,\xi,y,\eta)$	represents the kernel function
$G'(x,y,y)$	is the spanwise derivative of the chordwise integral evaluated at the downwash station

This form of the downwash equation has two singularities removed from the integrand such that the improper integrals, due to the dipole terms of the kernel function, are easily evaluated. However, the integrand contains an additional singularity that requires application of special integration techniques necessary to provide accurate downwash calculations.

An example of the singularity characteristic that exists at the downwash station is shown in figure 2 that presents a plot of an example of the spanwise integrand of equation (1).

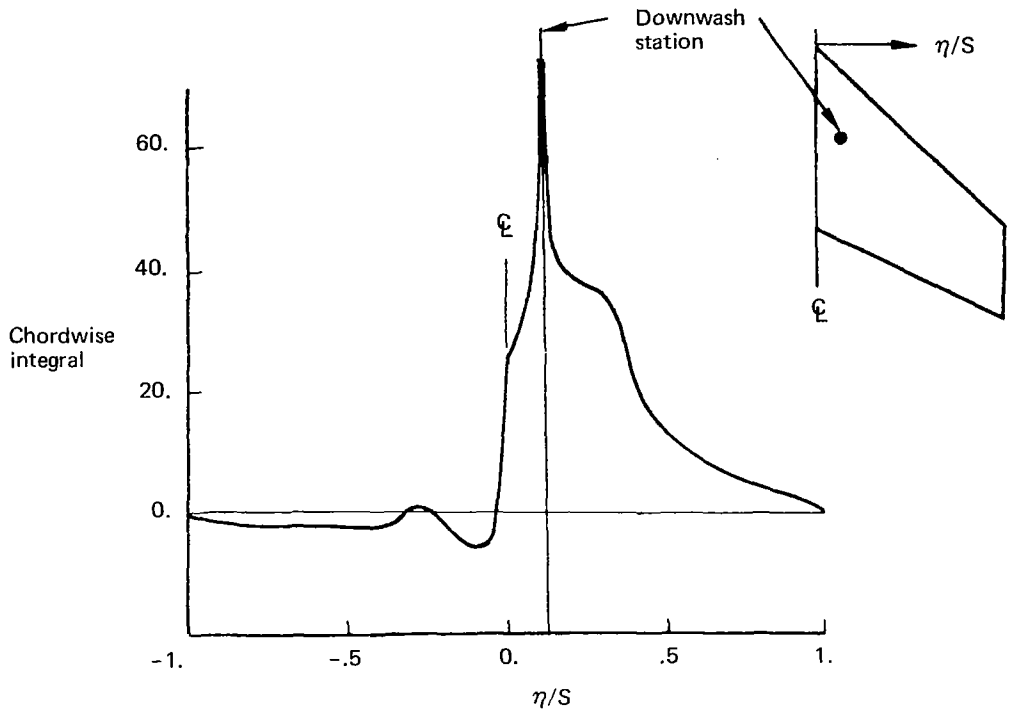

Figure 2.—Spanwise Variation of Integrand of Equation (1)

In NASA CR-2543, contribution of this singularity to the downwash is evaluated by applying suitable integration quadrature functions to a localized region around the downwash station. However, spacing requirements for spanwise integration stations in the very near vicinity of the downwash station impose severe accuracy restrictions on chordwise integrations.

Numerical investigations indicate that up to 40% of the computation time is consumed in applying this integration technique to evaluate the contribution of this singularity to the downwash.

Significant reductions in computer usage costs are achieved by reducing the number of spanwise integration stations required to evaluate the integrand in the near vicinity of the downwash station. Cost reductions result from changing the mathematical form of the integrand. The analytical expression describing the singularity and its strength is subtracted from the integrand and its downwash contribution is evaluated outside of the downwash integral. The analytical form of the singularity is obtained from downwash evaluations involving the singular part of the kernel function. Terms of the kernel function that contribute to the singularity expression are designated as the dipole term, the inverse square root term, and the logarithmic term as indicated in the following integral expressions.

$$I_1 = \int_{-s}^{s} \sqrt{s^2-\eta^2} \int_{x_\ell}^{x_t} \Delta P(\xi,\eta)\, e^{-ikx_0} \left[\frac{-1}{(y-\eta)^2} \left(1. + \frac{(x-\xi)}{\sqrt{(x-\xi)^2+\beta^2(y-\eta)^2}} \right) \right] d\xi d\eta \qquad (2)$$

dipole term

$$I_2 = \int_{-s}^{s} \sqrt{s^2-\eta^2} \int_{x_\ell}^{x_t} \Delta P(\xi,\eta)\, e^{-ik(x-\xi)} \frac{ik}{\sqrt{(x-\xi)^2+\beta^2(y-\eta)^2}}\, d\xi d\eta \qquad (3)$$

inverse square root term

$$I_3 = \int_{-s}^{s} \sqrt{s^2-\eta^2} \int_{x_\ell}^{x_t} \Delta P(\xi,\eta)\, e^{-ik(x-\xi)} \left(-\frac{k^2}{2} \right) \log \left[\sqrt{(x-\xi)^2+\beta^2(y-\eta)^2} - (x-\xi) \right] d\xi d\eta \qquad (4)$$

logarithmic term

The chordwise integrals are evaluated by forming a Taylor series expansion of $\Delta P(\xi, y)\, e^{-ik(x-\xi)}$ about the downwash station and inserting the expansion into the above integrals. The Taylor series expansion is given as:

$$\Delta P(\xi,y)\, e^{-ik(x-\xi)} \cong \Delta P(x,y) + (\xi-x) \left. \frac{\partial \left[\Delta P(\xi,y)\, e^{-ik(x-\xi)} \right]}{\partial \xi} \right|_{\xi=x} + \frac{(\xi-x)^2}{2} \left. \frac{\partial^2 \left[\Delta P(\xi,y)\, e^{-ik(x-\xi)} \right]}{\partial \xi^2} \right|_{\xi=x} + \cdots \qquad (5)$$

Insertion of equation (5) into equation (2) and performing the chordwise integration yields an expression for the spanwise integration given as:

$$I_1 = \int_{-s}^{s} \sqrt{s^2-\eta^2} \left[\frac{\beta^2}{2} \log(\beta^2(y-\eta)^2) \left. \frac{\partial \left[\Delta P(\xi,y) e^{-ik(x-\xi)} \right]}{\partial \xi} \right|_{\xi=x} - \frac{*\text{regular terms}}{(y-\eta)^2} \right] d\eta \quad (6)$$

The singularity due to the inverse square root term is obtained in a similar fashion that yields

$$I_2 = ik \int_{-s}^{s} \sqrt{s^2-\eta^2} \left[-\Delta P(x,y) \log(\beta^2(y-\eta)^2) + *\text{regular terms} \right] d\eta \quad (7)$$

The spanwise singularity contained in the third integral may be identified by redefining the logarithmic kernel function for values of $\xi < x$ as being

$$\log\left[\sqrt{(x-\xi)^2+\beta^2(y-\eta)} - (x-\xi)\right] = \log\beta^2(y-\eta)^2 - \log\left[\sqrt{(x-\xi)^2+\beta^2(y-\eta)^2} + x-\xi\right] \quad (8)$$

and inserting this into equation (4) provides the following singular expression

$$I_3 = -\frac{k^2}{2} \int_{-s}^{s} \sqrt{s^2-\eta^2} \left[\log(\beta^2(y-\eta)^2) \int_{x_\ell}^{x} \Delta P(x,y) e^{-ik(x-\xi)} d\xi + *\text{regular terms} \right] d\eta \quad (9)$$

The singularities are combined and subtracted out of the spanwise integrand and evaluated in closed form outside of the integral. The combined singularity strength is given as

$$T(x,y) = \frac{\beta^2}{2} \left. \frac{\partial \ \Delta P(\xi,y) e^{-ik(x-\xi)}}{\partial \xi} \right|_{\xi=x} - ik\Delta P(x,y) - \frac{k^2}{2} \int_{x_\ell}^{x} \Delta P(\xi,y) e^{-ik(x-\xi)} d\xi \quad (10)$$

* regular terms are nonsingular functions

Thus the singularity strength to be subtracted from the integrand is

$$\sqrt{s^2-\eta^2}\;\; T(x,y)\log\left[\beta^2(y-n)^2\right]$$

The closed form evaluation of this singularity using Mangler's technique of reference 4 is then given as

$$\int_{-s}^{s}\sqrt{s^2-\eta^2}\; T(x,y)\log\beta^2(y-\eta)^2 d\eta = \pi T(x,y)\left[\frac{s^2}{2}\log\left(\frac{\beta s}{2}\right)^2 - \frac{s^2}{2} + y^2\right] \quad (11)$$

The modified form of the downwash integral takes the final form given as follows:

$$\pi\left(\frac{w}{v}\right) = \int_{-s}^{s}\sqrt{s^2-\eta^2}\left\{\int_{x_\ell}^{x_t}\Delta P(\xi,\eta)\underbrace{\left[K(x,\xi,y,\eta)\right.}_{\text{singular}} + \underbrace{\left.K(x,\xi,y,\eta)\right]}_{\text{non-sing.}} d\xi\right.$$

$$+\frac{2}{(y-\eta)^2}\int_{x_\ell}^{x}\Delta P(\xi,y)\exp(-ik(x-\xi))d\xi - \frac{G'(x,y,y)}{y-\eta}$$

$$\left.-T(x,y)\log\beta^2(y-\eta)^2\right\} d\eta$$

$$+\pi\left\{2\int_{x_\ell}^{x}\Delta P(\xi,y)\exp(-ik(x-\xi))d\xi + yG'(x,y,y)\right.$$

$$\left.+ T(x,y)\left[\frac{s^2}{2}\log\left(\frac{\beta s}{2}\right) - \frac{s^2}{2} + y^2\right]\right\} \quad (12)$$

Numerical evaluation of the spanwise integrand of equation (12) is shown in figure 3 for the same analysis case of figure 2. The singularity is no longer present at the downwash station and the integrand in the vicinity of the downwash station can be easily evaluated using integration quadratures having only a small number of integration stations within this localized zone.

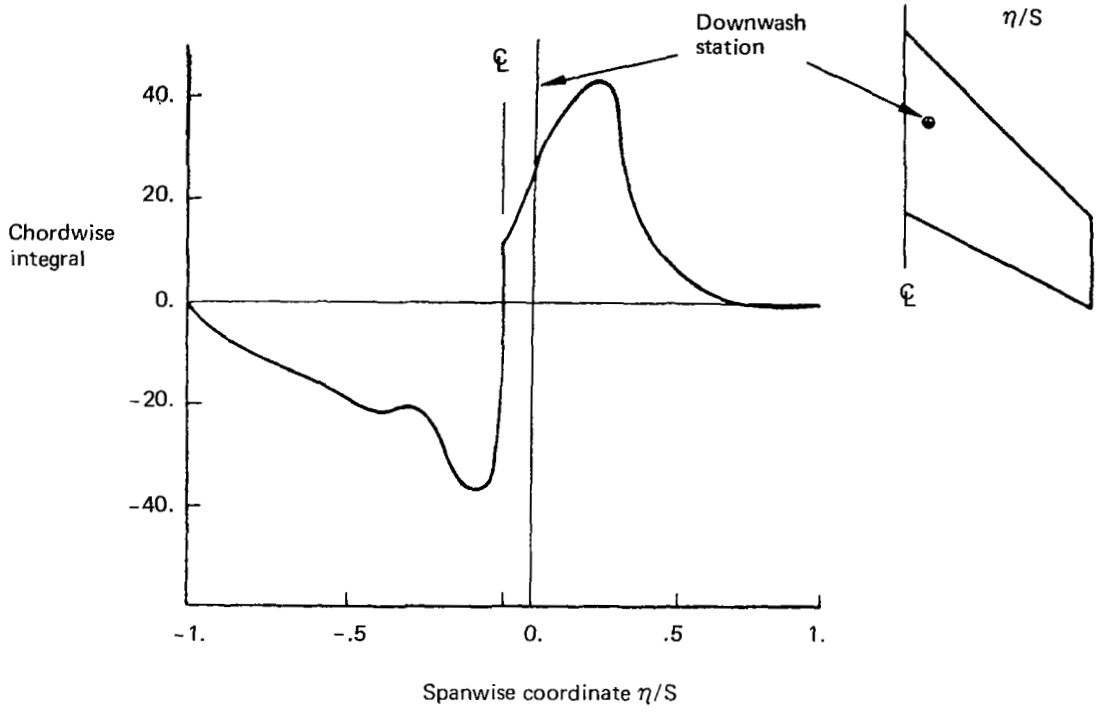

Figure 3.—Spanwise Variation of Integrand Defined in Equation (12)

This modification of the spanwise integrand has a significant effect in reducing the computing costs. However, this reduction in cost imposes restraints on the placement of collocation stations in the near vicinity of pressure discontinuities.

Figure 4 represents the chordwise downwash distribution for a configuration having a 20% chord control surface and applying the integration technique of evaluating the spanwise integral using suitable integration quadrature procedures. (See equation (1))

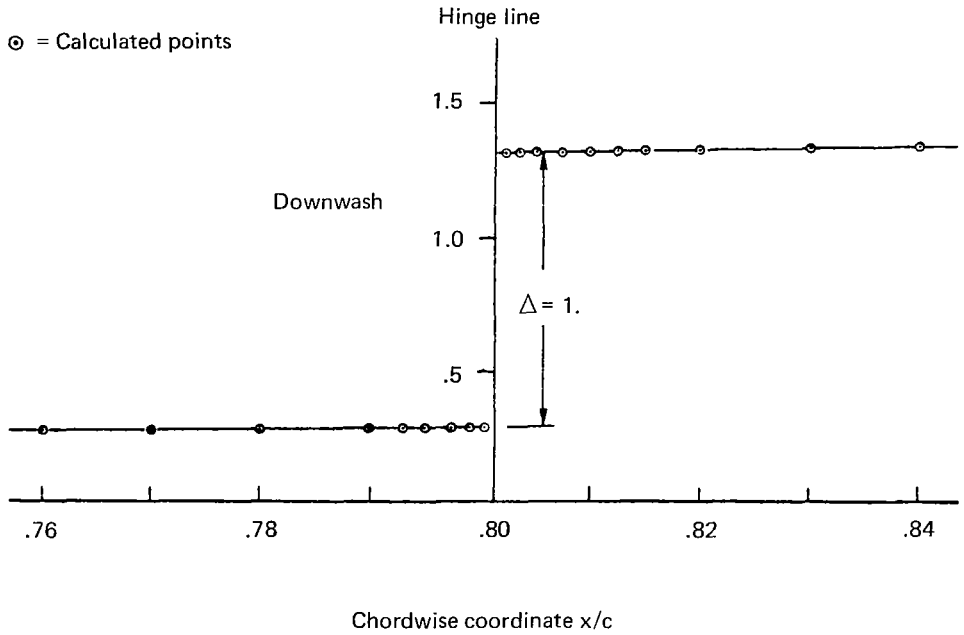

Figure 4.—Chordwise Downwash Distribution Obtained by Applying Method of Equation (1) (Singularities Evaluated by Appropriate Quadratures)

The downwash is smooth on either side of the hinge line and the discontinuity value across the hinge line matches the required discontinuity for unit rotation of the control surface. Use of this integration method does not impose any restriction on the placement of collocation stations in the near vicinity of the hinge line.

However, a restriction is required for the placement of collocation stations in the near vicinity of the hinge line when using the singularity subtraction procedure of equation (12). A downwash distribution obtained by using the integration method based on equation (12) is shown in figure 5.

Singularities appear at the hinge line coupled with some downwash waviness in the distributions over a small region away from the hinge line. The singularity at the hinge line is due to the inability of the Taylor series to properly represent the pressure function that contains a logarithmic singularity at the hinge line.

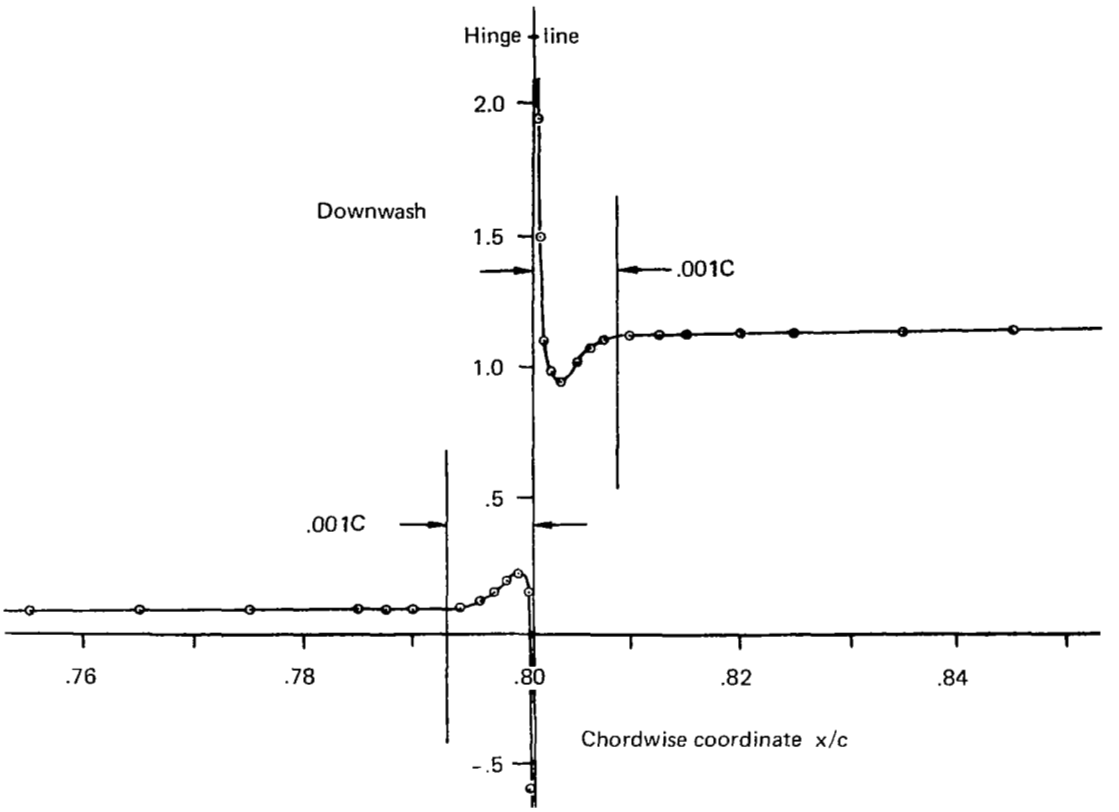

Figure 5.–Downwash Distribution Obtained Using Method of Equation (12) (Singularity Removed and Evaluated Separately)

It is recommended that the collocation stations are placed no closer to the hinge line than three-fourths of 1 percent local chord.

A spacing restriction is also recommended for the placement of collocation stations in the near vicinity of the leading edge when the procedure of equation (12) is used to evaluate the downwash distributions.

Downwash distribution of figure 6 indicates that the calculated downwashes become singular at the leading edge and that waviness in the distribution extends for a distance of 1½ percent of the local chord aft of the leading edge.

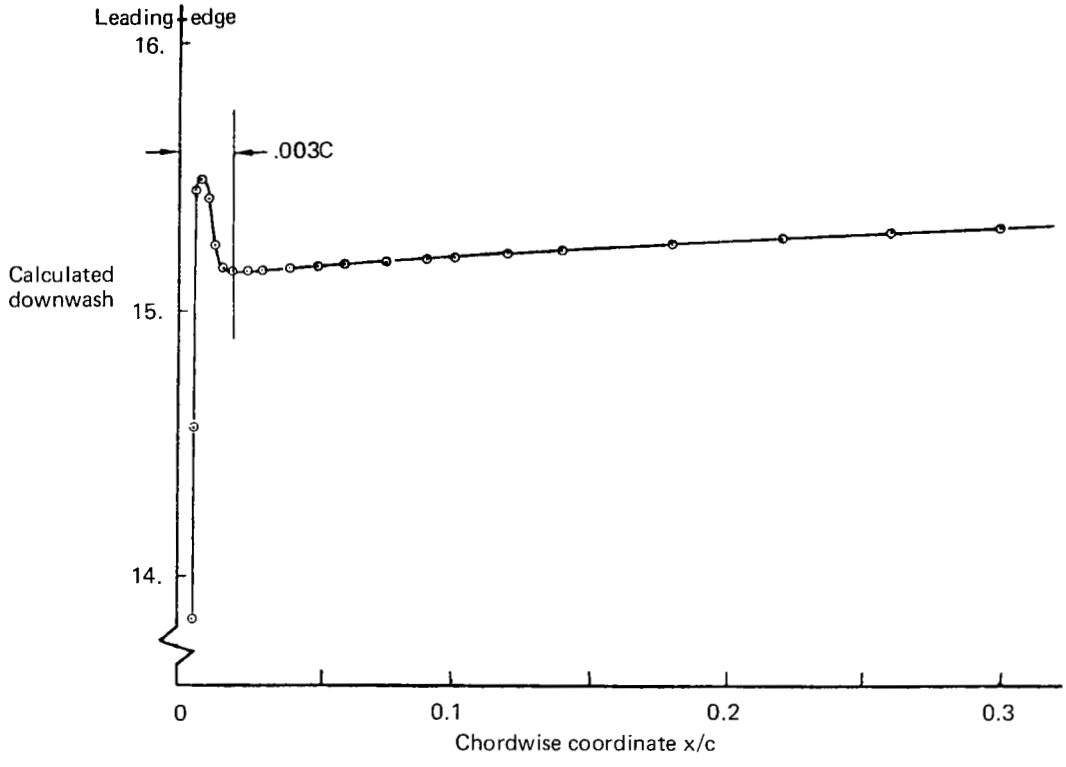

Figure 6.—A Calculated Downwash Distribution Near Leading Edge Using the Singularity Procedure of Equation (12)

Therefore, it is recommended that the downwash collocation stations are separated from the leading edge by a distance equal to or greater than 1½ percent of local chord.

Imposition of restrictions on the placement of collocation stations in the near vicinity of pressure singularities should not severely hamper user applications. Accurate predictions of unsteady loadings may be obtained provided that the collocation stations are not distributed within the above mentioned restriction regions.

REVISION OF SPANWISE LOADING FUNCTIONS

The solution process developed to obtain unsteady loadings over a lifting surface with discontinuous downwash distributions is initiated by developing a pressure distribution inducing downwash discontinuities that are identical with those contained in the kinematic downwash distribution. This downwash distribution is then subtracted from the kinematic downwash to provide a residual distribution that is smooth and continuous, for which the corresponding pressure distribution may be obtained by standard collocation procedures.

The key to this solution process is the development of pressure expressions that will exactly match the discontinuities in boundary conditions (downwash) along the edges of the control surface.

Pressure expressions that satisfy this requirement are presented in Appendix A and Appendix B for the leading and trailing edge control surface configurations, respectively. These pressure expressions are valid within localized regions of the discontinuities, but have not been matched with the planform edge boundary conditions. However, in prior work reported in reference 1, the pressure expressions defined for the discontinuous downwash regions have been extended to the limits of the planform. Boundary conditions were satisfied exactly by requiring the pressures to go to zero in proportion to the square root of the distance from the planform edges. For example, the pressure expressions developed for motions of a control surface located on the right-hand side of the planform are extended to the edges of the planform (including the left-hand planform region) and are then multiplied by other modifying functions such that the pressure is forced to zero in proportion to the square root of the distance from all the planform side edges.

Results of recent investigations indicate that this manner of extending the discontinuity pressures over the entire planform is a significant factor in requiring large computer times for application of the program of reference 1. Subsequent investigations have revealed that the spanwise and chordwise pressure distributions induced by downwash discontinuities are very localized to the regions of the discontinuities. Calculation of the downwash discontinuities depends only on the local pressure gradients and not on the overall level of the pressure distribution at large distances away from the discontinuities. Therefore, the calculation time may be reduced by defining the pressure expression only over localized regions of the planform.

A representative example, demonstrating that the discontinuity pressure expressions contain only localized gradients near the control surface side edges, may be obtained by

examining plots of the discontinuity pressure expressions. Figure 7 represents the sample planform having a control surface, displaying a single spanwise ray where the pressures have been calculated at the indicated circles due to motions of the right-hand side control surface. Figures 8 and 9 show the spanwise variations of in-phase (real) and out-of-phase (imaginary) parts, respectively, of the discontinuity related pressure function.

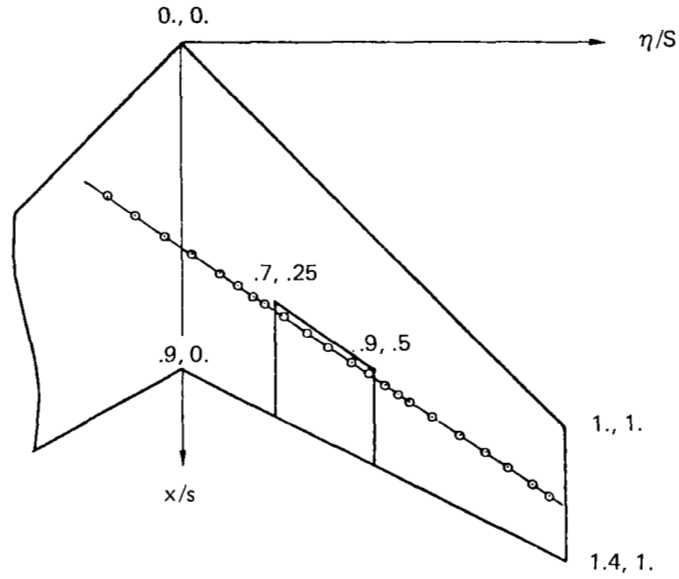

Figure 7.—Analysis Planform Used to Evaluate Pressure Variation

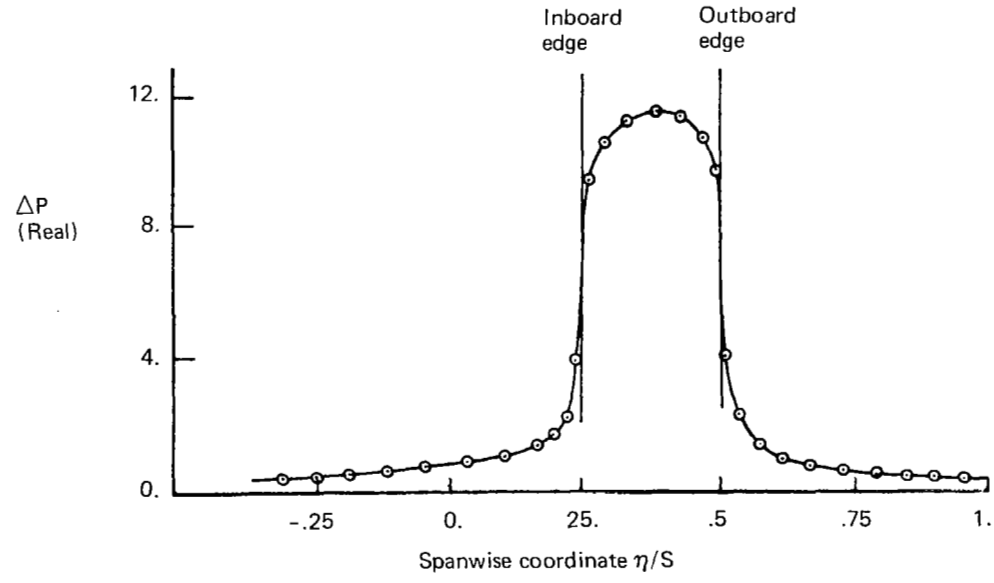

Figure 8.—In-Phase Part of Pressure Distribution

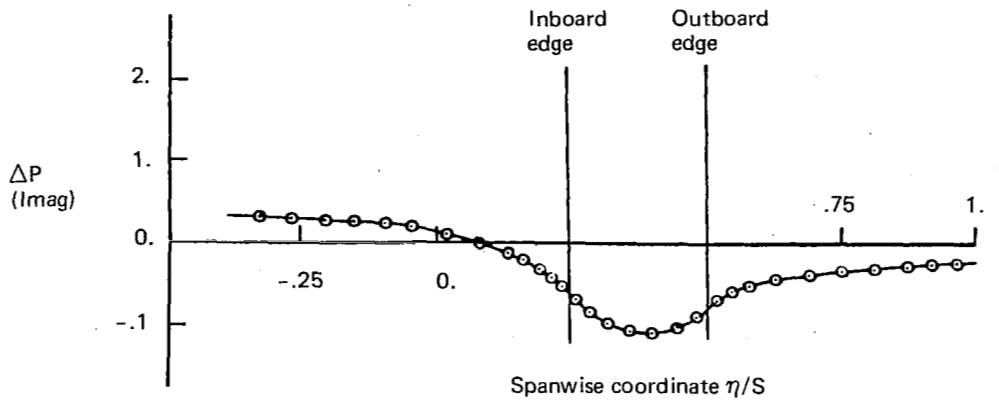

Figure 9.—Out-of-Phase Part of Pressure Distribution

Pressure distributions shown in figures 8 and 9 contain steep gradients near the control surface side edges and diminish to small and almost constant values at relatively small distances from the side edges.

It should be noted further that the pressures tend to become constant along chordwise stations located at relatively small distances away from the control surface side edges. This characteristic of having slightly varying chordwise distributions of pressure coupled with very small spanwise gradients, has the effect of raising or lowering the overall level of the discontinuity related pressure distribution, but does not contribute to the generation of the discontinuities required in downwash. Consequently, the spanwise pressure modification functions have been modified so that the pressures inboard of the control surface are reduced smoothly to zero beyond a relatively small distance from the inboard side edge. The function is constant over the length of the control surface to maintain the singularity strengths of the pressure distribution. The spanwise modification function at stations outboard of the control surface retains the original square root roll-off characteristics that were contained in the original development. The roll-off function inboard of the control surface has the characteristics of maintaining second derivative continuity at the end limits of the interval to ensure downwash continuity across the end stations of the interval. The length of the roll-off interval has been selected on the basis of minimizing undesirable fluctuations of downwash caused by the spanwise gradient of the roll-off function.

MODIFICATION OF SPANWISE INTEGRATION ALGORITHM

The integration algorithm developed for the computer program described in NASA CR-2543 has been modified to provide increased accuracy and more efficient computational integration procedures in predicting unsteady loadings due to control surface motion.

An integration algorithm has been developed for analysis of a basic lifting surface with various combinations of leading edge and/or trailing edge control surfaces. Control surfaces may be located anywhere along the leading or trailing edges.

Descriptions of the integration procedures are presented in the following subsections.

BASIC LIFTING SURFACE ALGORITHM

The procedure applied in developing a cost effective integration algorithm consists of subdividing the total spanwise integration interval (extending from the left-hand wingtip to the right-hand wingtip) into subintervals having end points at local maxima of the integrand of equation (12) and at discontinuities of the integrand, with a minimum number of internal stations in each subinterval to meet a specified accuracy requirement.

This obviously requires a positive identification of all peak values and discontinuities of the integrand.

Locations of peak values and discontinuities of the integrand are dependent upon sweep angle, aspect ratio, taper ratio, Mach number, reduced frequency, number of downwash chords and the chordwise distribution of downwash stations.

Typical spanwise integrands, following chordwise integration, are shown in figure 10 and figure 11 for a highly swept planform. These variations result from a combination of the first chordwise pressure mode (defined as $\sqrt{(x_t - x)/(x - x_\ell)}$) and ninth spanwise pressure mode (defined as $\sin(17 \cos^{-1}(-\eta/s))$) for M = .9, k = 1.0, and a downwash station located at y/s = 0.10.

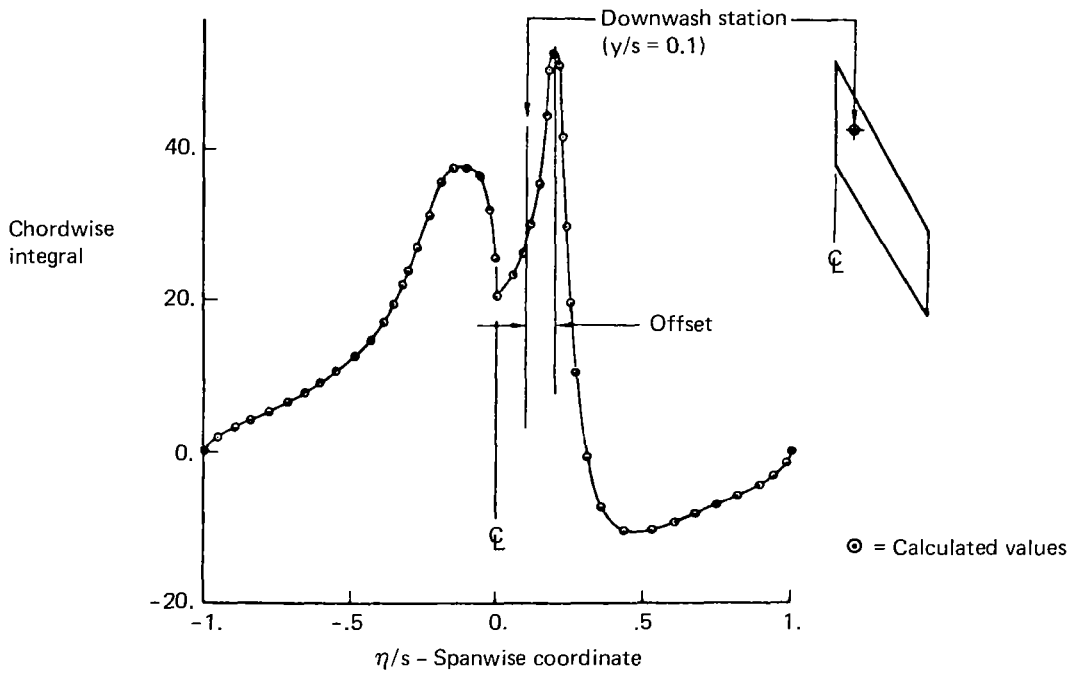

Figure 10.—Real Part of Integrand of a Swept Planform Analysis at M = .9, k = 1.

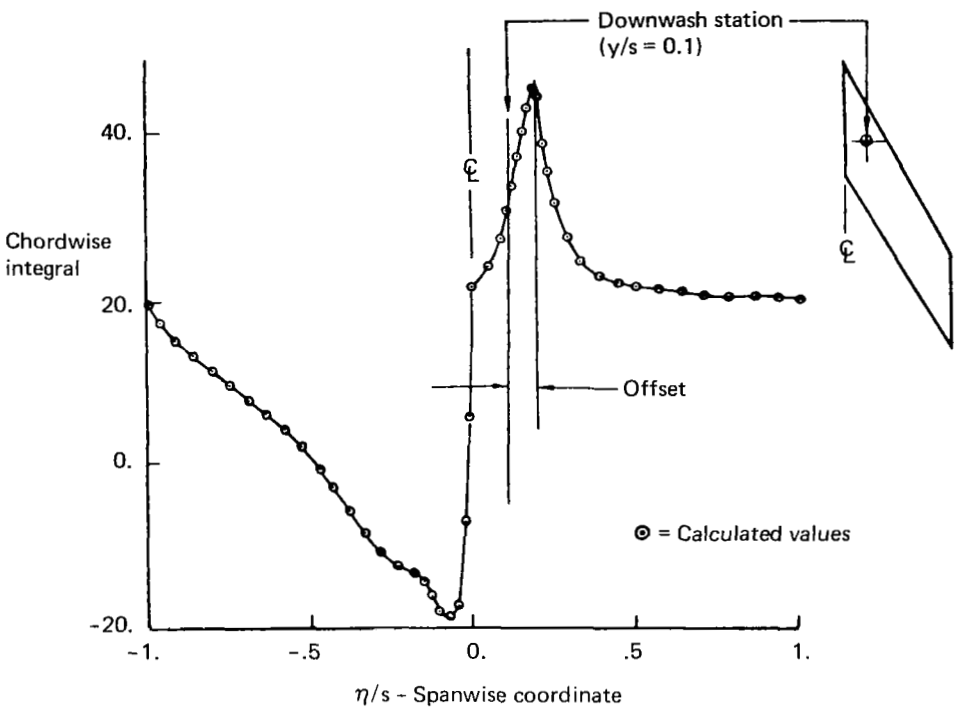

Figure 11.—Imaginary Part of Integrand of a Swept Planform Analysis at M = .9, k = 1.

The integrand plots of figure 10 and figure 11 exhibit a slope discontinuity at the planform centerline. Also a peak value occurs just outboard of the downwash station, and the integrand sometimes exhibits an oscillatory character in the vicinity of the downwash station.

The oscillatory character integrand is apparent in figure 12, which is derived from the same parameters just identified with the exception that the downwash station is located far away from the planform centerline. The distribution shown in figure 12 also exhibits a slope discontinuity at the centerline, a high gradient loading outboard of the downwash chord, and an oscillatory character in regions adjoining the downwash station.

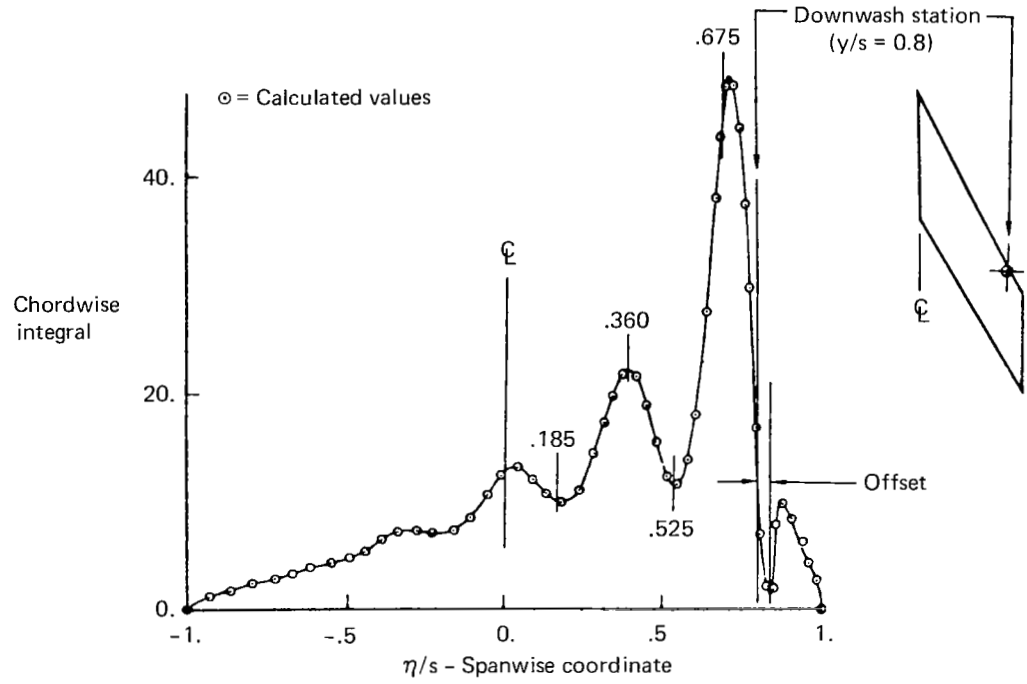

Figure 12.—Real Part of Integrand of a Swept Planform Analysis Having a Downwash Station at y/s = 0.8

The slope discontinuity in loadings at the planform centerline is due to the discontinuities in direction of the leading and trailing edges at the planform centerline.

The oscillatory character of the spanwise integrand is due to the waviness of the spanwise pressure mode. The particular spanwise pressure mode used in these analyses is the highest order mode that would be retained in an analysis with nine downwash chords.

The ninth spanwise pressure term is given by

$$\Delta P(\eta) = \sin (2N-1)\theta = \sin 17\theta \qquad (N=9)$$

where $\theta = \cos^{-1}(-\eta/s)$

The comparison of the ninth spanwise pressure mode plot, shown in figure 13 with the results of figure 12, indicates that there is a one-to-one correspondence between peak values of the integrand plot and of the pressure distribution.

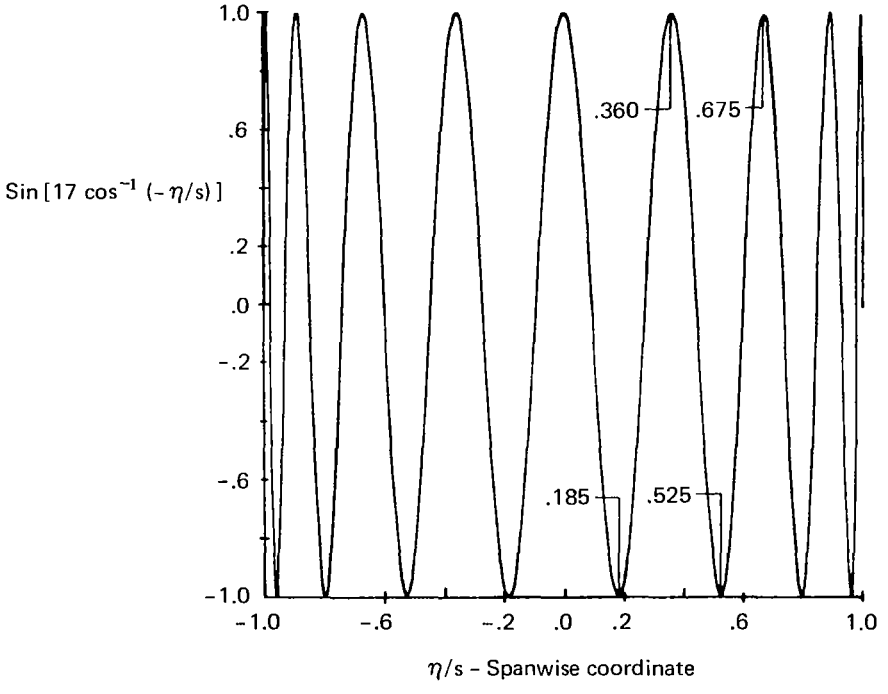

Figure 13.—Distribution of Ninth Spanwise Pressure Mode

The only datum remaining to be identified (prior to subdividing the integration interval) is the loading station offset from the downwash station shown in figure 10.

Cause of the high gradient loadings at stations outboard of the downwash station may be traced to the combined effects of planform sweep and kernel function characteristics.

The particular term of the kernel function associated with high gradient loadings is the dipole term, defined as

$$K_{dp} = \frac{-1}{(y-\eta)^2}\left[1+\frac{x-\xi}{\sqrt{(x-\xi)^2+\beta^2(y-\eta)^2}}\right]$$

where

x = chordwise coordinate of the downwash station

y = spanwise coordinate of the downwash station

ξ = chordwise coordinate of the pressure station

η = spanwise coordinate of the pressure station

$\beta^2 = 1 - M^2$

M = Mach number

For simplicity, the $\frac{-1}{(y-\eta)^2}$ term is omitted in the following discussion.

The simplified expression for the downwash integrand takes the form

$$I_{dw} = \int_{\ell e}^{te} \Delta P(\xi,\eta)\left[1+\frac{x-\xi}{\sqrt{(x-\xi)^2+\beta^2(y-\eta)^2}}\right] d\xi$$

Wherein $\Delta P(\xi, \eta)$ is the assumed pressure loading function described in terms of planform coordinates having zero values ahead of the leading edge and finite values on the planform.

The kernel function is described in cartesian coordinates and exists over the infinite plane $z = 0$.

For high Mach number cases, the simplified form of the kernel function has a value that is slightly less than 2.0 for stations ahead of the downwash station and a value slightly greater than zero for stations downstream of the downwash station.

Thus, the integrand of the chordwise integral (formed by the product of the pressure loading and kernel function) is relatively large for regions ahead of x and much smaller for regions downstream of x. For swept planforms, the large loadings of the chordwise integrand is confined to that portion of the planform ahead of x and extending spanwise to the intersection of the leading edge. Chordwise integrand loadings take on very small values at spanwise stations located outboard of the leading edge intersection. Thus, the integrand of the spanwise downwash integral has rapid change in value in the near vicinity of the leading edge, where the leading edge is intersected by the x-coordinate line through the downwash station.

The station of rapid loading change is near the leading edge, but not exactly on the leading edge, except for those cases where the shortened form of the kernel function becomes

$$K_{dp} = \left[1 + \frac{x-\xi}{|x-\xi|}\right] \qquad \text{for } \eta = y$$

An example of the spanwise integrand variation for a swept planform in steady flow is presented in figure 14. The downwash station is located at 10% of the chord length aft of the leading edge and has a spanwise coordinate of y/s = 0.40. The chordwise pressure mode is defined as $\sqrt{(x_t - x)/(x - x_\ell)}$, and a spanwise pressure mode is defined as $\sqrt{1 - (\eta/s)^2}$ with M = .9, and k = 0.0.

Initial inspection suggests that the first derivative of the spanwise integrand may have a discontinuity just outboard of the downwash station. However, an enlargement, shown in figure 15, indicates that the curve is smooth and continuous. Further investigations indicate that the distribution becomes more rounded as the downwash station is moved further aft of the leading edge. A plot of locations of the maximum values of the downwash integrand is shown in figure 16 for downwash stations located on the y/s = 0.4 downwash chord.

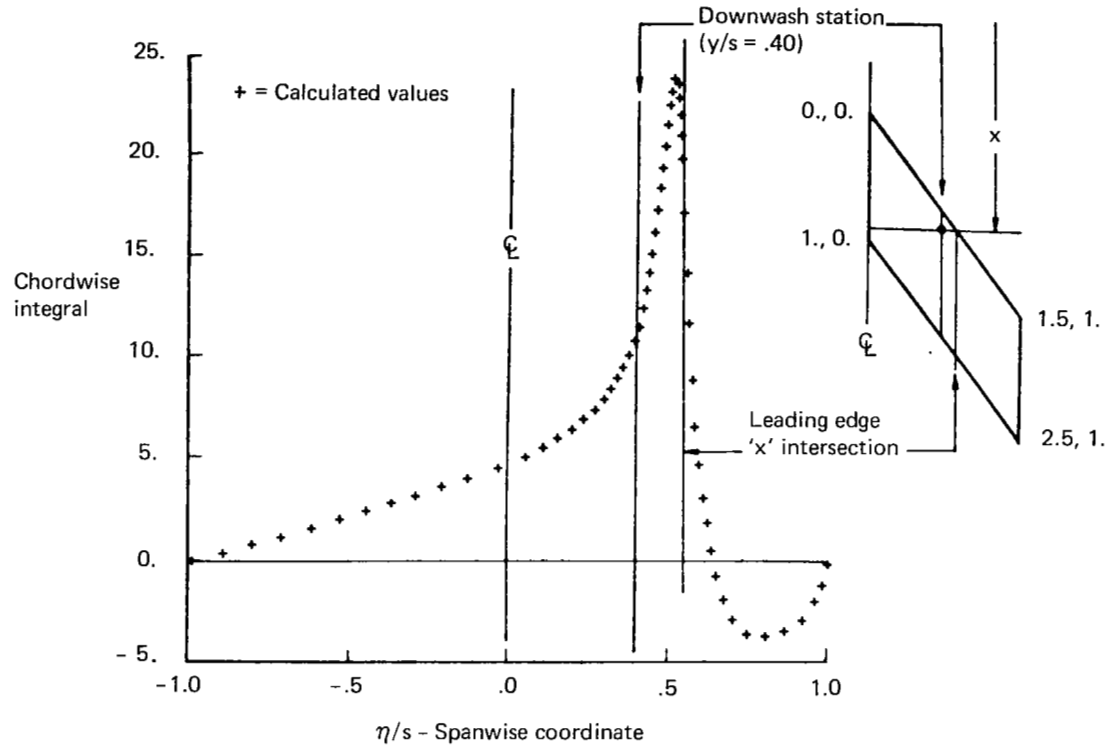

Figure 14.—Distribution of Spanwise Integrand in Steady Flow at M = .9

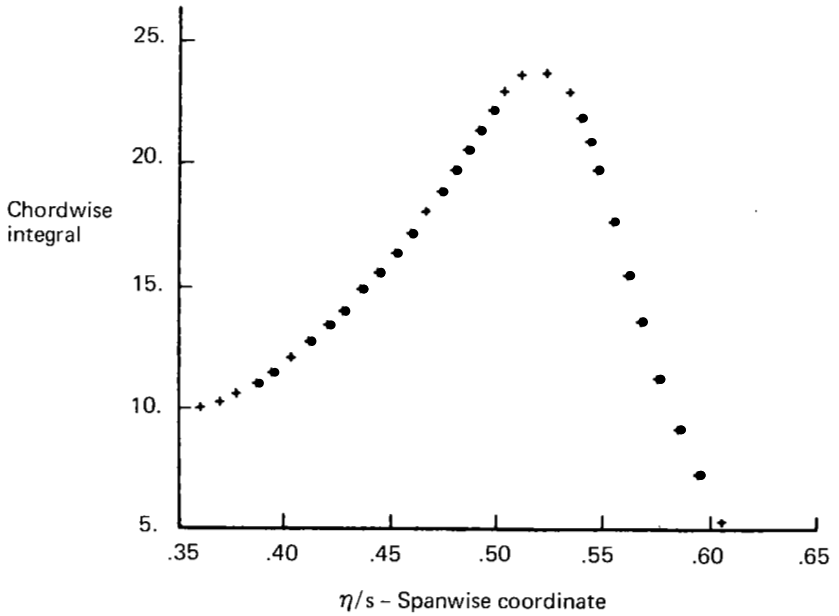

Figure 15.—Enlargement of Critical Loading Region of Figure 14

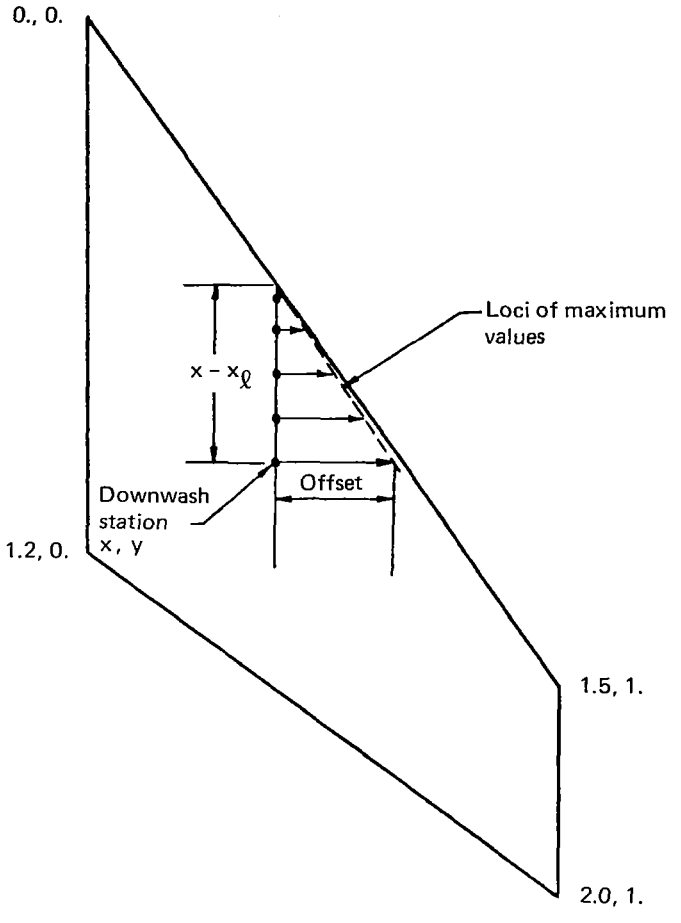

Figure 16.—Location of Maximum Integrand Values for a Downwash Chord at y/s = .40

Results of numerical investigatons indicate that the offset distance is not affected by variations in reduced frequency but is Mach-number dependent in accordance with the relationship

$$\frac{1.19}{1+\beta^2}\left[1.0+.03\left(1-\frac{M^2}{.81}\right)\right]$$

where all offsets are referenced to the offsets obtained for the case of M = .9.

Graphically obtained offset distance definitions required for the arbitrary sweep angle case are provided in figure 17.

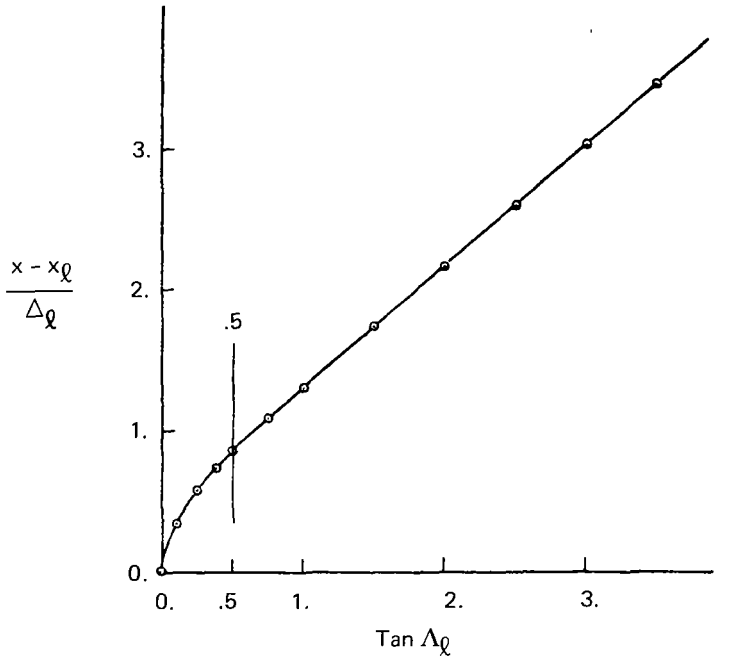

Figure 17.—Offset Distance Definition as Function of Sweep Angle

Offset distances applicable to configurations having leading edge sweep angles equal to or greater than $\Lambda_\ell \geqslant \tan^{-1}(.5)$ are given by

$$\Delta_\ell = (x-x_\ell) \Big/ \left\{ \left[\frac{1.19}{1+\beta^2} \right] \left[1.+.03\left(1-\frac{M^2}{.81}\right) \right] \left[.86786(\tan\Lambda_\ell - 1.)+1.30 \right] \right\}$$

Offset distance for configurations having sweep angles less than $\Lambda_\ell < \tan^{-1}(.5)$ is given by

$$\Delta_\ell = (x-x_\ell) \Big/ \left\{ \left[\frac{1.19}{1+\beta^2} \right] \left[1.+.03\left(1-\frac{M^2}{.81}\right) \right] \right.$$

$$\left. * \left[4\tan\Lambda_\ell - 6\tan^2\Lambda_\ell + 4\tan^3\Lambda_\ell \right] \left[.86786 \right] \right\}$$

Offset distances for downwash stations located in the near vicinity of a swept trailing edge are obtined from the leading edge offset definitions by replacing x_ℓ by x_t and tan Λ_ℓ by tan Λ_t.

Once the stations of peak loadings and loading discontinuities have been identified, the total integration interval is subdivided into subintervals with end points located at the critical loading stations. Checks are made to ensure that no more than one inflection point is contained in any subinterval to obtain sufficient accuracy with low order integration quadrature formulas.

Results of numerical investigations indicate that the downwash integrand becomes increasingly oscillatory and more difficult to integrate as the location of the downwash station approaches the region near the intersection of the trailing edge with the planform centerline.

Figure 18 represents a plot of the integrand obtained for a downwash station located near the trailing edge at a spanwise station of y/s = .0826 for M = 0.90 and k = 2.5.

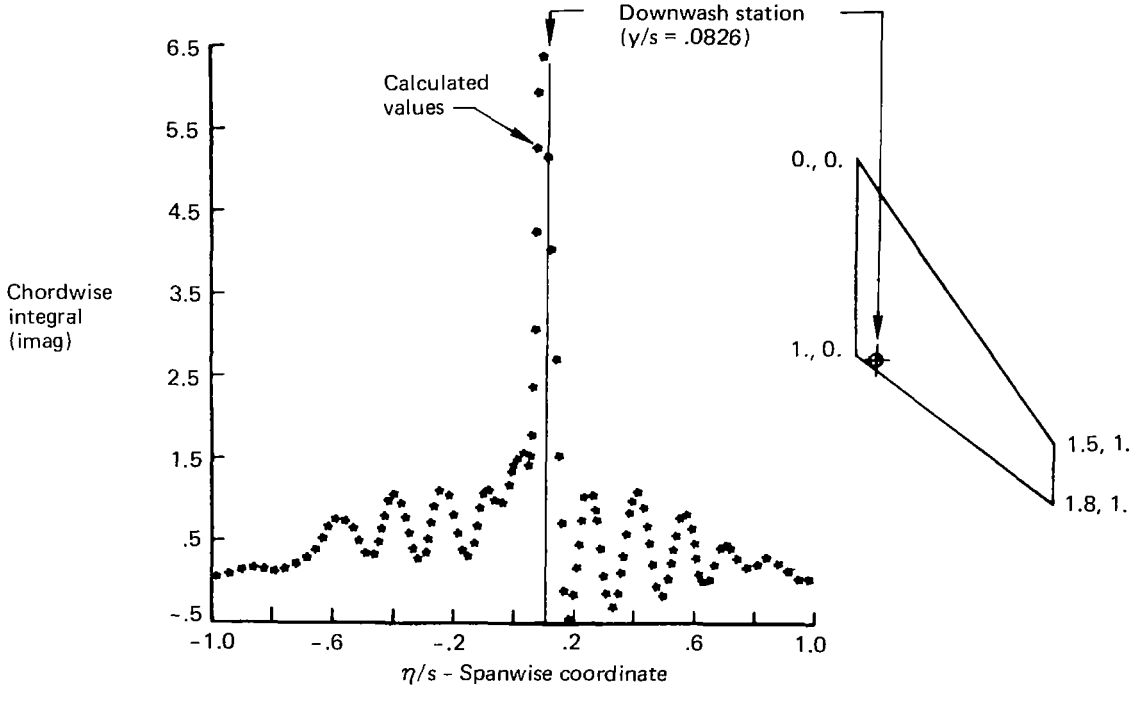

Figure 18.—Spanwise Integrand for a Downwash Station Located Near Trailing Edge in Midspan Region for M = .9, k = 2.5

An estimation of the maximum error that results for this highly swept configuration is obtained by comparing a set of precise downwash calculations with values obtained from the present integration algorithm.

The set of 'precise' downwash calculations is obtained by subdividing the total integration interval into many subintervals and applying a high order quadrature rule in each subinterval. Results of the 'precise' integration are presented in table 1, representing a column of the downwash matrix having nine spanwise and six chordwise pressure terms. The 108 entries in table 1 are listed in the order

$(1,1)_R$ $(1,1)_I$ $(1,2)_R$ $(1,2)_I$ $(1,3)_R$ $(1,3)_I$ $(1,4)_R$ $(1,4)_I$

$(1,5)_R$ $(1,5)_I$ $(1,6)_R$ $(1,6)_I$ $(1,7)_R$ $(1,7)_I$ $(1,8)_R$ $(1,8)_I$

$(1,9)_R$ $(1,9)_I$ $(2,1)_R$ $(2,1)_I$ ——— ———

——— ——— ——— ———

$(6,8)_R$ $(6,8)_I$ $(6,9)_R$ $(6,9)_I$

wherein $(m,n)_R$, $(m,n)_I$ represent the real and imaginary downwash components associated with the m'th chordwise and the n'th spanwise pressure modes.

Table 2 represents downwash values obtained by the present integration algorithm.

Differences between corresponding entries in the two tables provide a measure of the maximum error in downwash calculation that is to be expected in the analysis of highly swept planforms for high subsonic Mach numbers and large values of k.

It is to be noted that the present integration algorithm allows any combination of spanwise and chordwise pressure terms to be used provided that the product of numbers of spanwise and chordwise terms does not exceed 72, and the number of chordwise terms does not exceed 8.

Table 1.—High Precision Downwash Matrix Obtained for the Configuration of Figure 18 with M = .9, k = 2.5 (Nine Spanwise and Six Chordwise Pressure Terms)

---REAL---	---IMAG---	---REAL---	---IMAG---	---REAL---	---IMAG---	---REAL---	---IMAG---
1.024E+01	-4.138E+00	-8.222E+00	4.805E+00	4.851E+00	-5.846E+00	-1.079E+00	6.755E+00
-2.405E+00	-7.108E+00	5.410E+00	6.823E+00	-7.930E+00	-6.237E+00	9.834E+00	5.850E+00
-1.078E+01	-5.992E+00	4.742E+00	-7.470E+00	-3.304E+00	6.708E+00	8.681E-01	-5.234E+00
1.952E+00	3.122E+00	-4.722E+00	-5.899E-01	7.333E+00	-1.924E+00	-9.750E+00	3.802E+00
1.181E+01	-4.490E+00	-1.321E+01	3.717E+00	-5.823E+00	-1.307E+01	5.785E+00	1.175E+01
-5.623E+00	-9.313E+00	5.255E+00	6.042E+00	-4.724E+00	-2.331E+00	4.239E+00	-1.371E+00
-3.980E+00	4.648E+00	4.025E+00	-7.251E+00	-4.373E+00	9.147E+00	-4.164E+00	1.080E+01
3.530E+00	-1.062E+01	-2.334E+00	1.020E+01	7.093E-01	-9.509E+00	1.160E+00	8.516E+00
-3.035E+00	-7.246E+00	4.736E+00	5.785E+00	-6.131E+00	-4.319E+00	7.126E+00	3.074E+00
2.285E+00	-6.466E+00	-2.227E+00	6.445E+00	2.088E+00	-6.413E+00	-1.842E+00	6.331E+00
1.492E+00	-6.139E+00	-1.046E+00	5.789E+00	5.565E-01	-5.224E+00	-6.592E-02	4.383E+00
-3.738E-01	-3.237E+00	-2.178E+00	5.159E+00	2.136E+00	-5.025E+00	-2.056E+00	4.748E+00
1.943E+00	-4.336E+00	-1.776E+00	3.840E+00	1.541E+00	-3.259E+00	-1.215E+00	2.593E+00
8.231E-01	-1.841E+00	-3.780E-01	1.009E+00				

Table 2.—Downwash Matrix Obtained by Present Integration Algorithm for the Configuration of Figure 18 with M = .9, k = 2.5 (Nine Spanwise and Six Chordwise Pressure Terms)

---REAL---	---IMAG---	---REAL---	---IMAG---	---REAL---	---IMAG---	---REAL---	---IMAG---
1.024E+01	-4.150E+00	-8.221E+00	4.790E+00	4.862E+00	-5.845E+00	-1.078E+00	6.774E+00
-2.417E+00	-7.104E+00	5.403E+00	6.810E+00	-7.915E+00	-6.245E+00	9.841E+00	5.866E+00
-1.080E+01	-5.982E+00	4.741E+00	-7.484E+00	-3.300E+00	6.694E+00	8.781E-01	-5.234E+00
1.952E+00	3.142E+00	-4.735E+00	-5.877E-01	7.329E+00	-1.936E+00	-9.736E+00	3.794E+00
1.181E+01	-4.472E+00	-1.323E+01	3.725E+00	-5.822E+00	-1.308E+01	5.789E+00	1.174E+01
-5.613E+00	-9.311E+00	5.253E+00	6.062E+00	-4.737E+00	-2.332E+00	4.238E+00	-1.383E+00
-3.967E+00	4.644E+00	4.029E+00	-7.234E+00	-4.392E+00	9.153E+00	-4.163E+00	1.079E+01
3.540E+00	-1.064E+01	-2.328E+00	1.021E+01	7.054E-01	-9.492E+00	1.146E+00	8.516E+00
-3.032E+00	-7.259E+00	4.749E+00	5.786E+00	-6.132E+00	-4.305E+00	7.110E+00	3.077E+00
2.291E+00	-6.479E+00	-2.216E+00	6.436E+00	2.095E+00	-6.408E+00	-1.853E+00	6.347E+00
1.482E+00	-6.146E+00	-1.040E+00	5.779E+00	5.670E-01	-5.220E+00	-7.037E-02	4.395E+00
-3.886E-01	-3.237E+00	-2.170E+00	5.151E+00	2.151E+00	-5.031E+00	-2.054E+00	4.749E+00
1.930E+00	-4.327E+00	-1.783E+00	3.833E+00	1.549E+00	-3.266E+00	-1.208E+00	2.600E+00
8.158E-01	-1.833E+00	-3.892E-01	1.007E+00				

ALGORITHM FOR CONFIGURATIONS WITH CONTROL SURFACES

The algorithms for configurations with control surfaces have been constructed to provide accurate predictions of unsteady loadings for control surfaces of arbitrary size and location along the leading and/or trailing edges.

Extensive use has been made of field plots to define the locations of peak loadings or loading discontinuities in spanwise plots of the downwash integrand (equation (12)). Field plots of critical loading locations are developed from plots of the integrand for a mesh of downwash stations distributed over the planform.

The planform is divided into zones (figure 19) wherein the integrand plots have similar characteristics for all downwash stations in the zone.

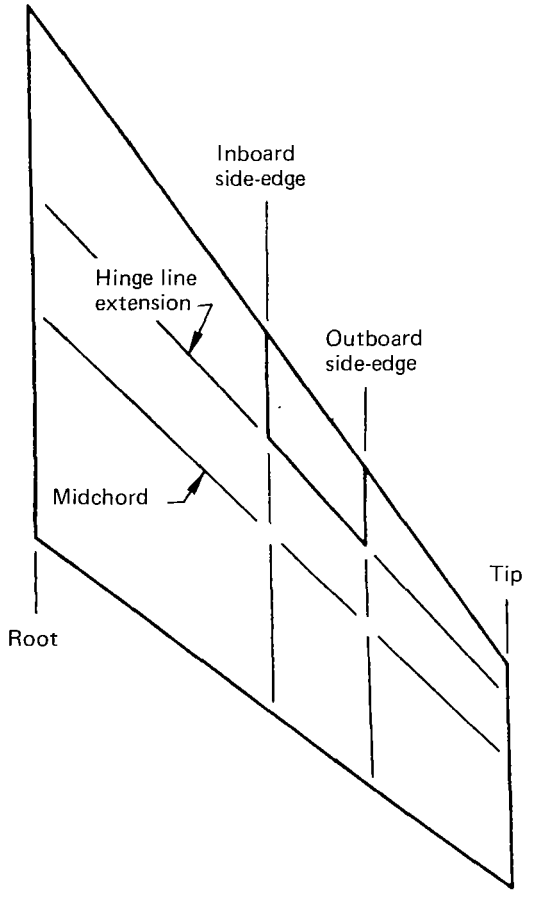

Figure 19.—Subdivision of Planform into Zones Having Similar Downwash Integrand Characteristics

Spanwise locations of critical loading stations for a specific zone are superimposed on the sketch of the planform. Stations with similar characteristics are joined by line segments to form a curve to denote the manner in which the critical loading locations vary over the surface of the planform.

A typical field plot of critical loading stations developed for downwash stations located inboard and aft of the control surface is shown in figure 20, wherein the outline of the planform and control surface is denoted by solid lines and the critical loading stations are denoted by dashed line segments.

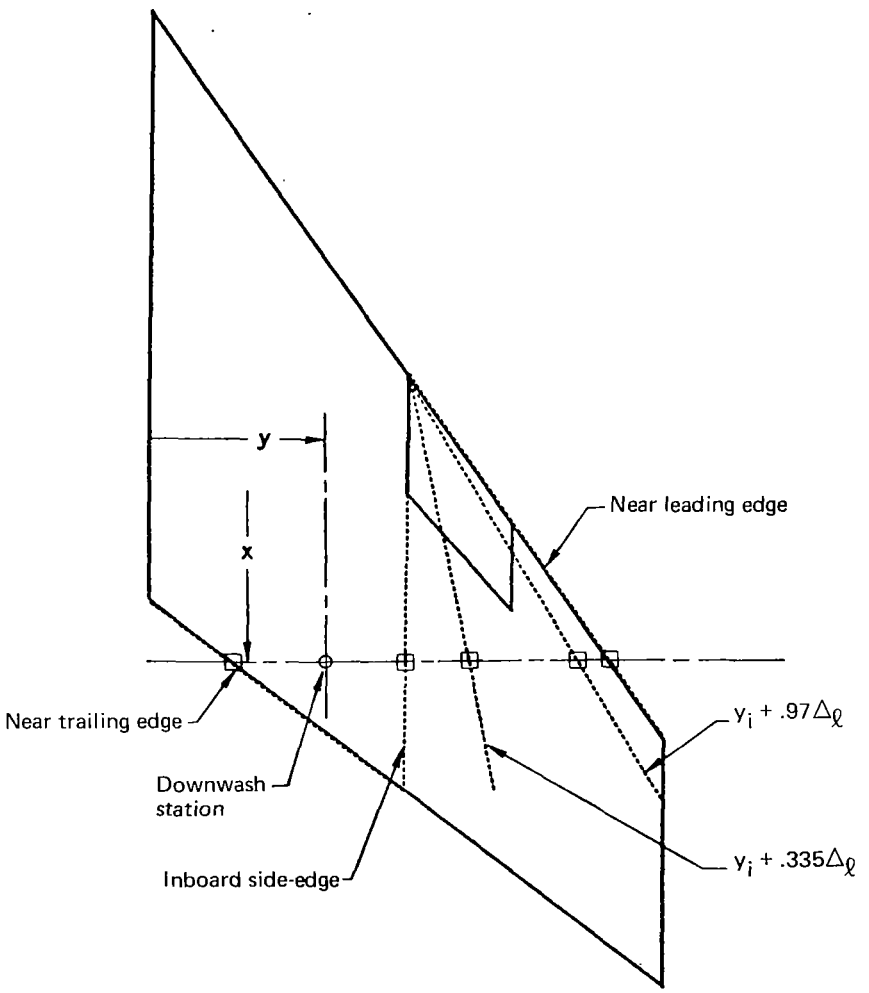

Figure 20.—Field Plot of Critical Loading Locations for a Downwash Zone that is Inboard and Aft of the Control Surface

The end points of the spanwise integration subintervals were determined from the intersection of the x coordinate (of the downwash station) with the critical loading locations as indicated by the square symbols in figure 20.

Field plots of the critical loading stations were developed in a similar manner for the remaining zones, and the process was repeated for several variations in the spanwise locations of the control surface to ensure that all critical loading stations have been adequately identified.

Field plot results of various swept planform investigations were combined to define interval subdivision required to satisfy accuracy criteria for an arbitrarily shaped control surface configuration.

A final check was performed to ensure that the spanwise waviness of the downwash integrand, in any interval, is compatible with accuracy for the order of integration polynomial being assigned to that length of interval.

REVISION OF THE CHORDWISE PRESSURE MODIFICATION FUNCTION

Cost reductions may be achieved by reducing waviness of residual downwashes so that only a small number of collocation stations are required to obtain accurate predictions of unsteady loadings for small span control surface configurations.

Analysis results of small percent chord control surface configurations indicate that the number of collocation stations available may be insufficient to obtain converged solutions when applying the method of NASA CR-2543.

Numerical analyses have been conducted to check solution convergence of small percent chord control surface configurations shown in figure 21, composed of a 20% chord aileron and a 6% chord tab.

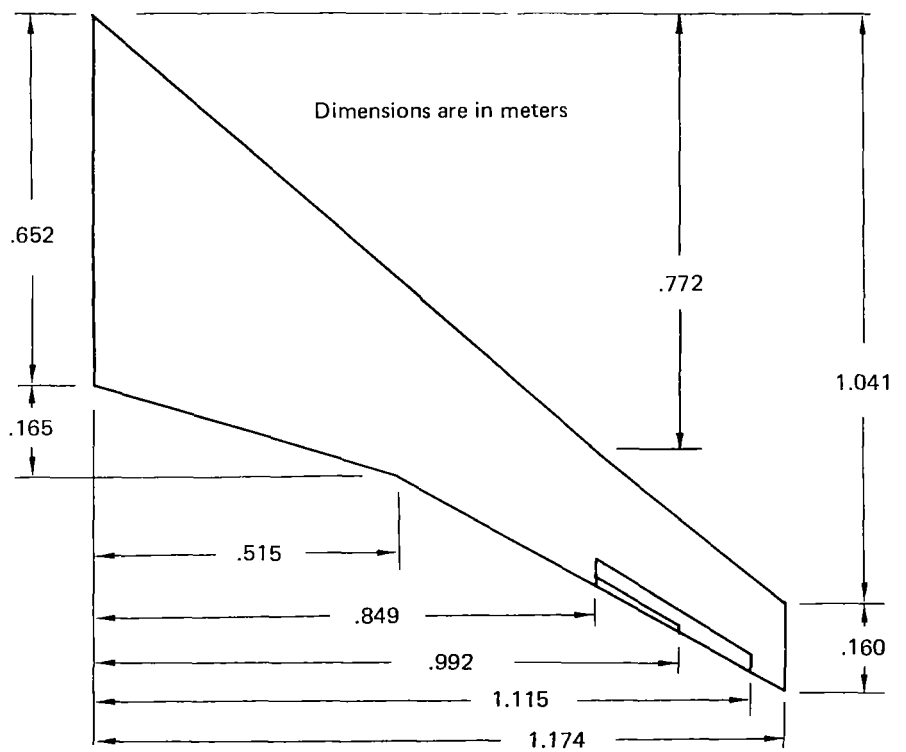

Figure 21.—Analysis Planform Used to Check Solution Convergence of Small Chord Control Surface Configurations

Figure 22 represents the chordwise pressure distribution obtained for a fixed rotation of the 20% chord aileron. The predicted pressure distribution contains a chordwise waviness that is not realistic when compared with experimental data. The pressure distribution near the hinge line appears to have the proper smoothness. However, there is an obvious reversal in the curvature of the distribution in the region between the leading edge and the hinge line.

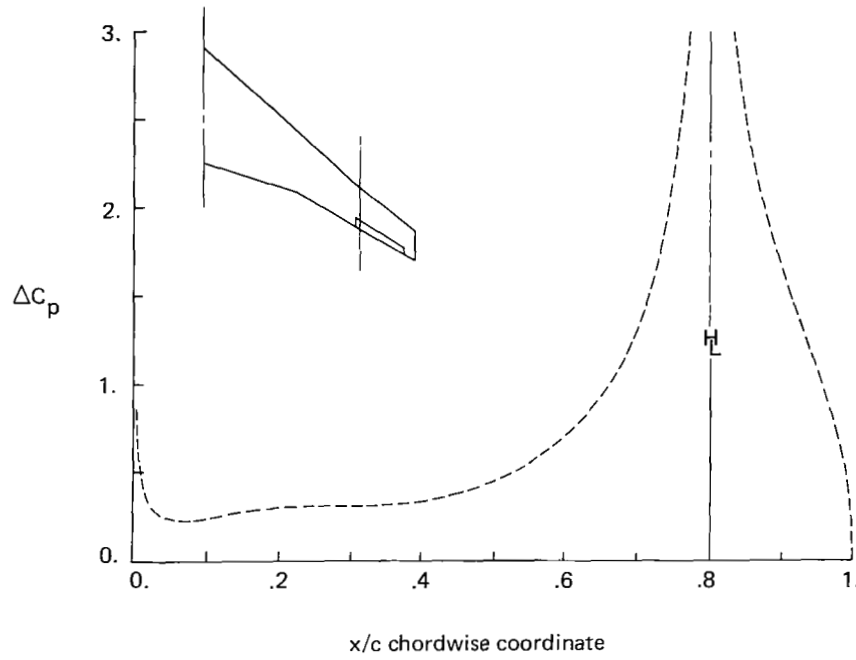

Figure 22.—Steady State Pressure Distribution Due to Deflection of 20% Chord Control Surface

Waviness of the chordwise pressure distributions is more pronounced in figure 23 which represents the steady state analysis results of the 6% chord control surface configuration of figure 21. The analysis results of figure 23 were obtained using the maximum chordwise number of downwash stations allowed by the program.

It appears that small length fluctuations are being caused by localized waviness in the residual downwash distributions. Localized waviness in the residual downwash distribution may cause the solution to be sensitive to the number of downwash stations used in the analysis.

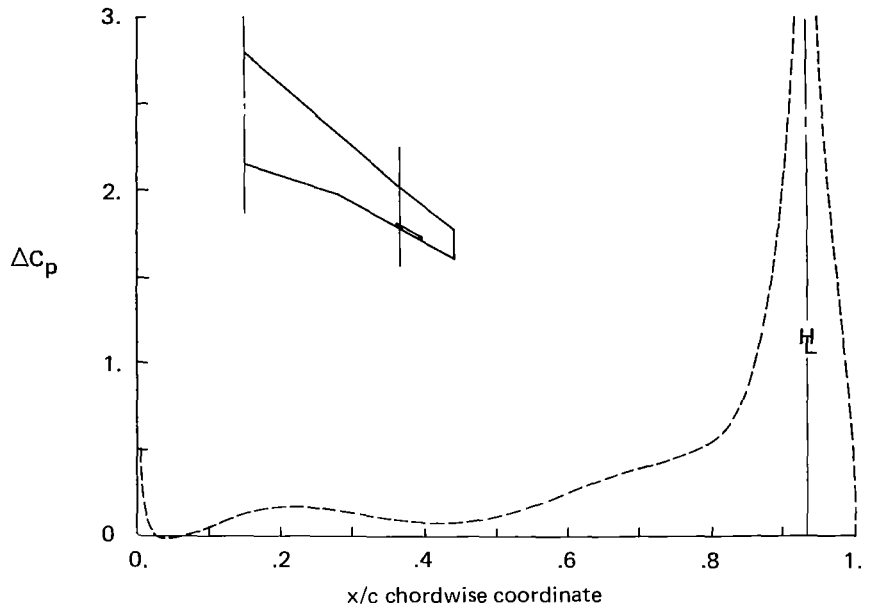

Figure 23.—Steady State Pressure Distribution Due to Deflection of 6% Chord Control Surface

The solution process is graphically displayed in figure 24 to indicate the technique used to predict unsteady loadings caused by control surface motions. The procedure consists of: 1) obtaining a kinematic downwash distribution from the definition of the modal displacements; 2) generating a discontinuous downwash distribution having discontinuities that are identical to those in the kinematic distribution; 3) forming a residual distribution by subtracting the generated discontinuous distribution from the kinematic distribution; 4) obtaining lifting surface pressures that satisfy the boundary conditions defined by the residual downwash distribution; 5) defining the total pressure distribution over the surface by summing the pressures required to generate the discontinuous downwash distribution with the pressures that satisfy the boundary conditions defined by the residual downwash distribution.

Smooth residual downwash that is free of localized waviness will provide solutions that are relatively insensitive to the number and distribution of downwash stations on the lifting surface.

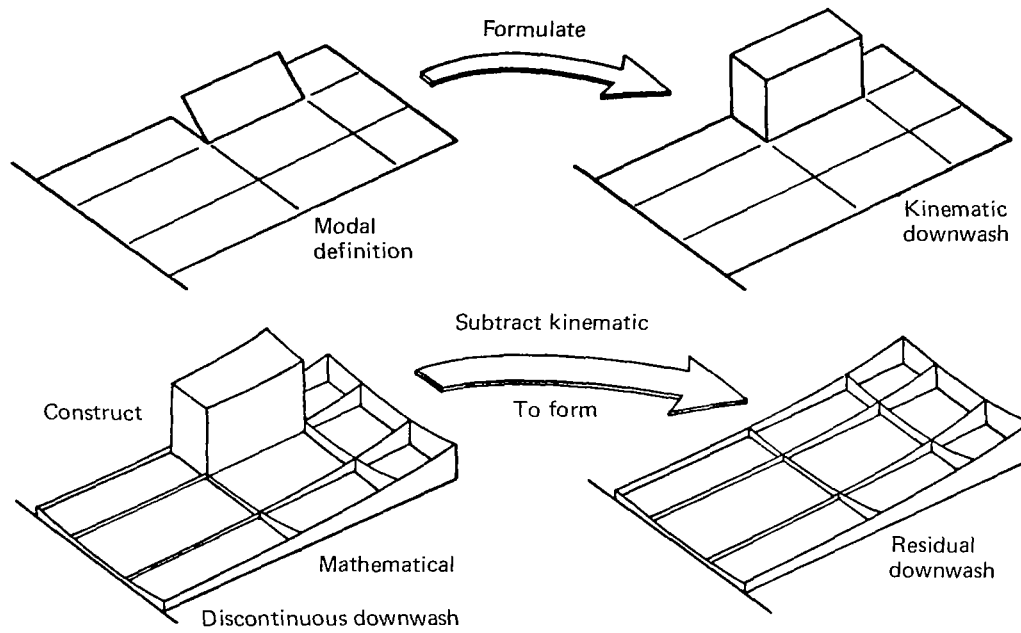

Figure 24.—Solution Process Applied to Trailing Edge Control Surface Analysis

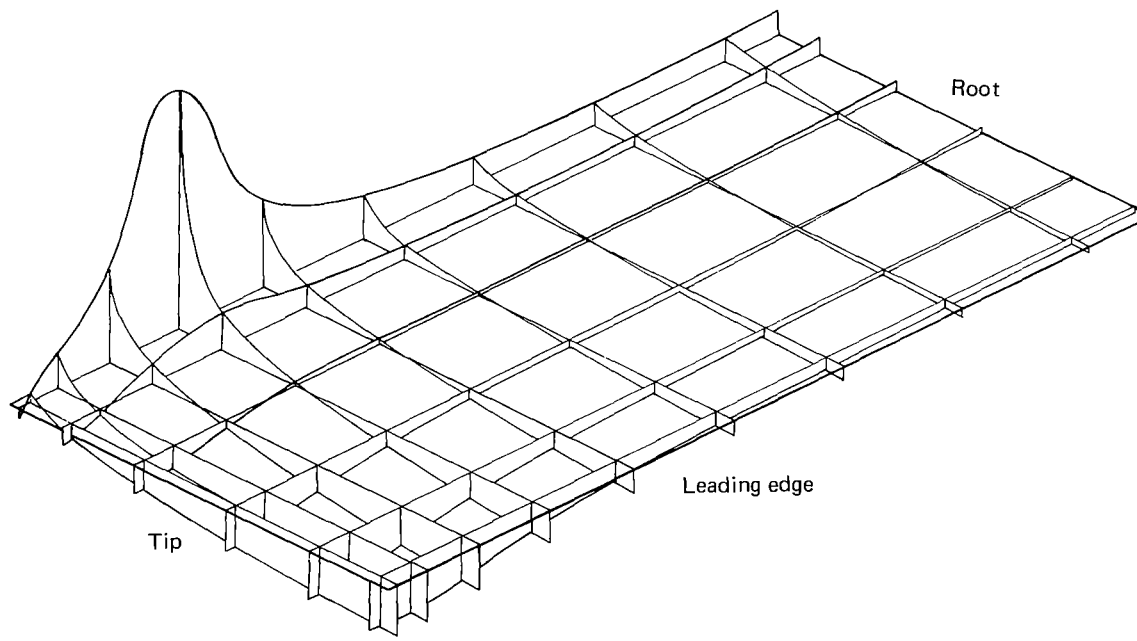

Figure 25.—Residual Downwash Distribution Obtained for Analysis of 6% Chord Control Surface Configuration

Figure 25 represents the residual downwash distribution resulting from analysis of the 6% chord control surface configuration. The large gradients present in both the chordwise and spanwise directions are evidently so severe that it is difficult to obtain converged solutions with the limited number of downwash stations available in the program.

The cause of the large gradients generated in the downwash distribution has been traced to the chordwise pressure modification function that is used to satisfy the planform edge boundary conditions. The modificaton function has the characteristics of forcing the incremental pressures to approach zero in proportion to the square root of the distance from the leading and trailing edges, as shown in figure 26. The modification function also maintains a value of unity at the hinge line along with zero slope to ensure proper evaluation of downwash discontinuities. The large chordwise curvatures that are generated in the region aft of the hinge line, within analyses of small percent chord control surface configurations, are responsible for the large gradient downwash distributions shown in figure 25.

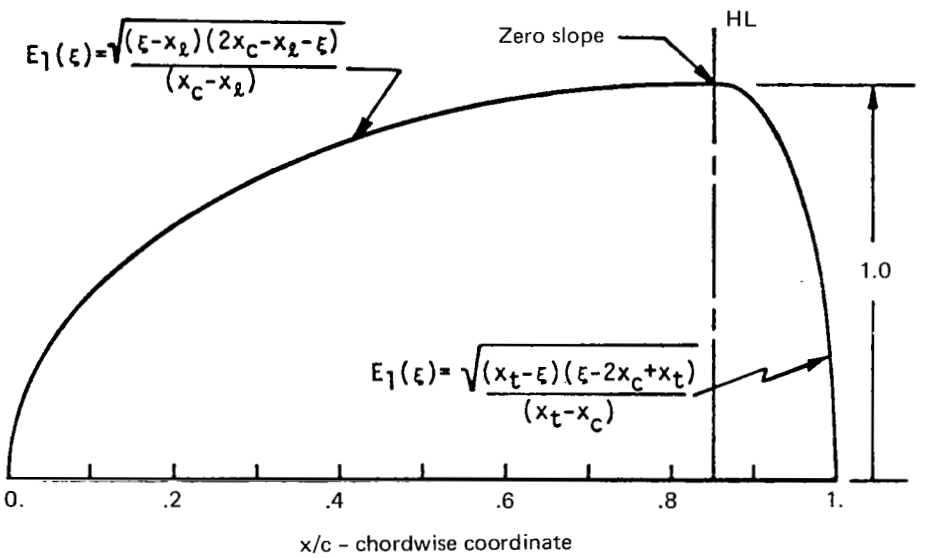

Figure 26.—Chordwise Pressure Modification Function

The chordwise pressure modification function has been revised and has the characteristics shown in figure 27.

The trailing edge boundary condition is satisfied by subtracting a function formed by the product of the trailing edge pressure term multiplied by a chordwise term that approaches a value of unity in proportion to the square root of the distance from the trailing edge.

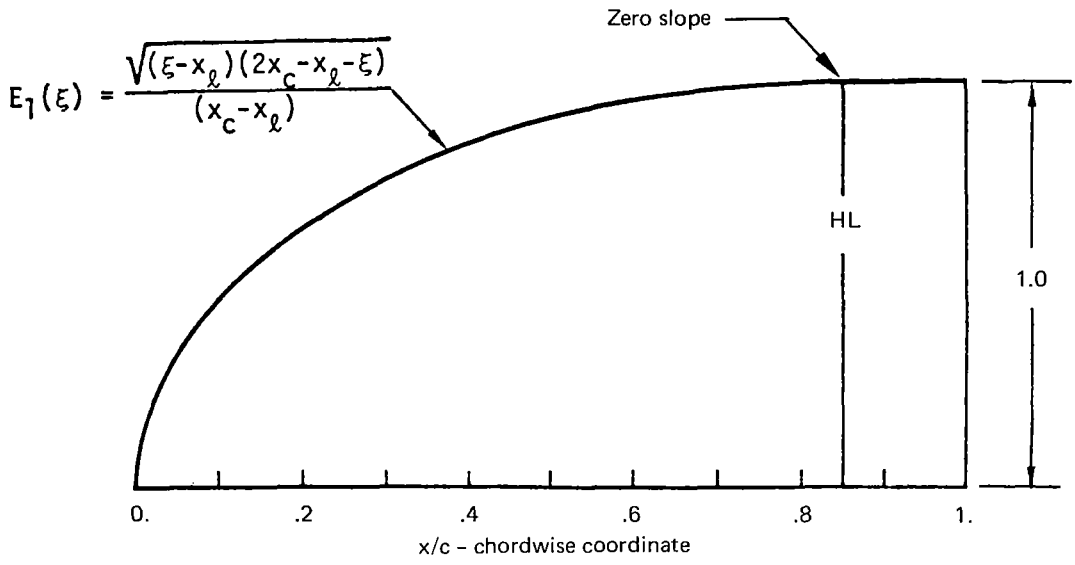

Figure 27.—Revised Pressure Modification Function

Residual downwash distributions obtained using the revised modification function are presented in figure 28 for the same analysis case that provided the results in figure 25. The highly localized downwash variations of figure 25 that prevented solution convergence are no longer present in figure 28.

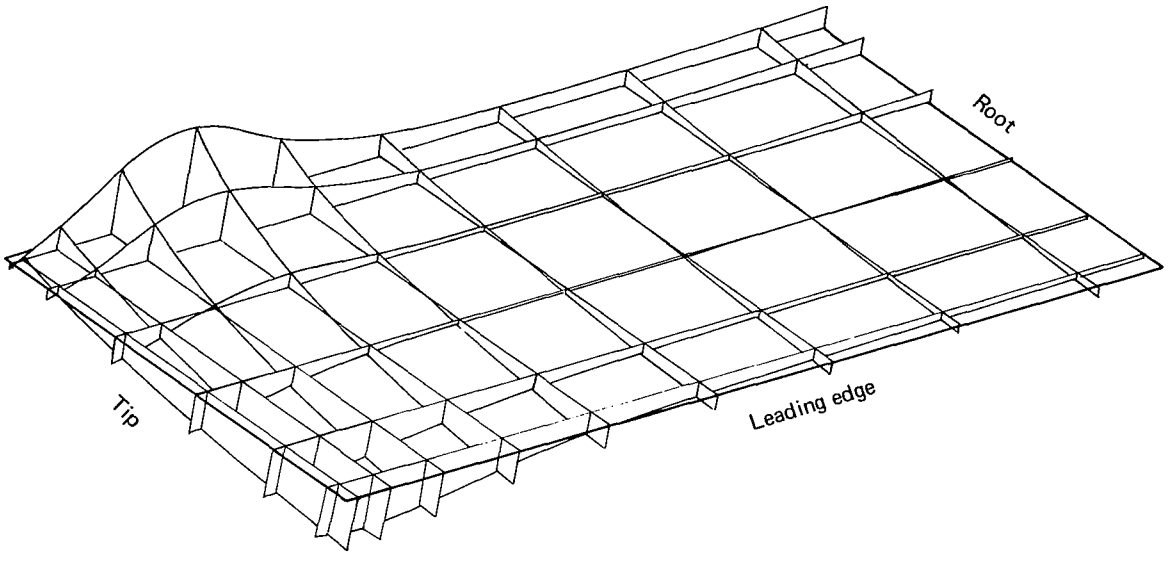

Figure 28.—Residual Downwashes Obtained in Analysis of 6% Chord Control Surface Using the Revised Modification Function

Comparisons of the pressure distributions that result from using the two modification functions in analysis of the small percent chord control surface configurations are shown in figure 29 and figure 30.

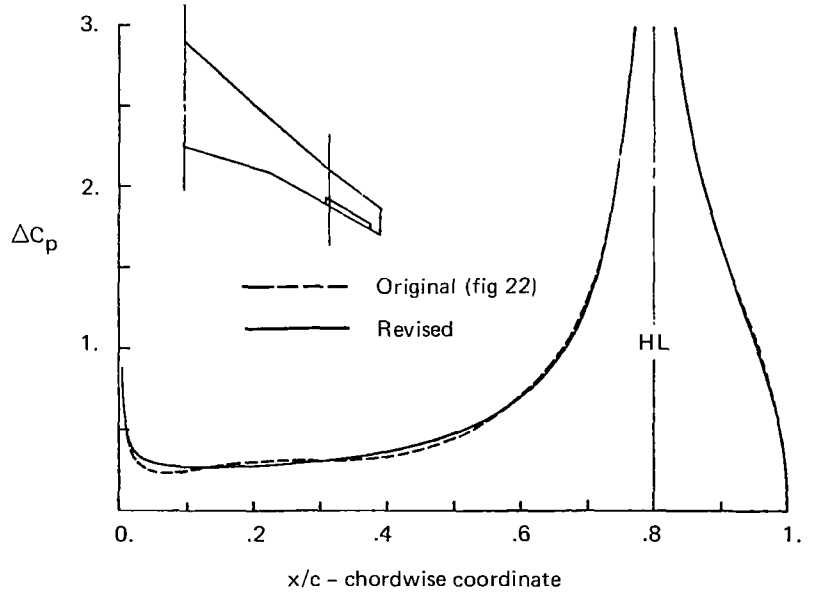

Figure 29.—Comparison of Pressures Obtained for Original and Revised Modification Functions—20% Chord Control Surface

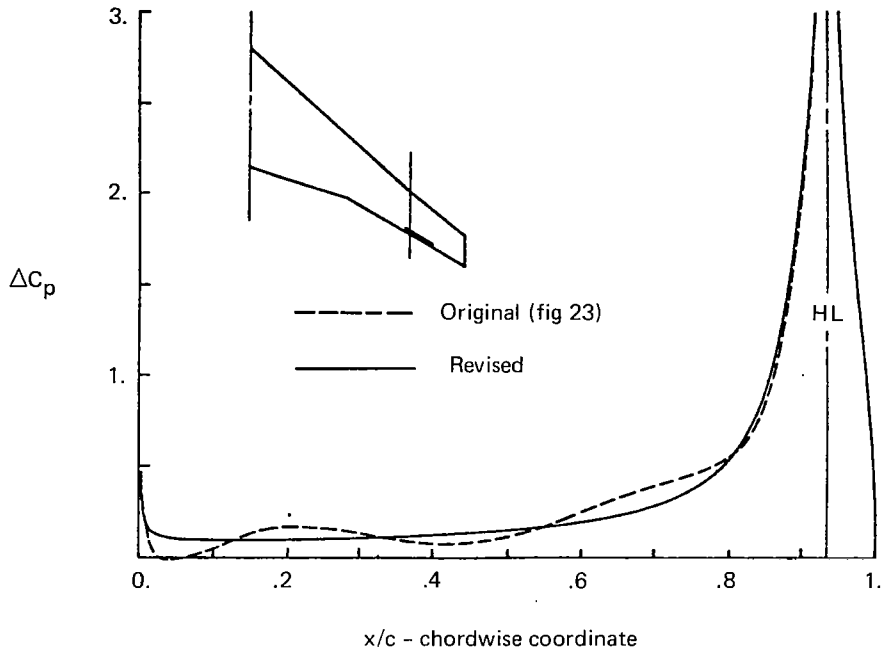

Figure 30.—Comparison of Pressures Obtained for Original and Revised Modification Functions—6% Chord Control Surface

Pressure distributions resulting from applying the revised modification function are smoothly varying and do not exhibit any reversal in curvature. The theoretical distributions take on characteristics similar to those observed in experimental results.

Solution convergence has been evaluated to determine the minimum chordwise number of downwash statons necessary to provide a converged solution for the analysis case of the 6% chord control surface configuration. Results of the investigation indicate that converged solutions may be achieved for this particular analysis case by using only five downwash stations distributed over each downwash chord.

Previous analysis results using the original modification function indicate that convergence cannot be attained even when the maximum number of eight chordwise downwash stations is used in the analysis.

Consequently, significant reductions in computer costs can now be gained by taking advantage of the smoother residual downwash distributions that result from this revision of the chordwise pressure modification function.

RESULTS AND TIMING COMPARISONS

This section contains comparisons of theoretical and experimental data that result from analyses and tests of four wing-control surface configurations. The experimental configurations consist of: 1) a swept wing having a full span flap (reference 7); 2) a swept wing having a partial span control surface (reference 8); 3) a swept wing having oscillating side-by-side control surfaces (reference 6); 4) a highly swept delta wing having leading edge and trailing edge control surfaces (references 9 and 10).

Theoretical pressure distributions are provided for a subsonic transport-type wing and control surface configuration to demonstrate the use of higher order spanwise pressure terms in analyses of highly swept configurations.

Computer timing results are provided for each of the above analysis cases. Computer usage costs (given in CP seconds) were obtained for the original program reported in NASA CR-2543 (reference 1) and also for the present prediction method. An estimation of the reduction in computer usage cost is obtained by comparing the CP seconds required for the two methods. All results were obtained on a CDC Cyber 175 computer having an FTN compiler with the optimization option set to 2.

STEADY-STATE RESULTS FOR FULL-SPAN FLAP CONFIGURATION

The full-span flap configuration of reference 7, for which measured pressures were obtained with various combinations of flap deflection and angle of attack, is shown in figure 31. The flap deflection and wing angle of attack were maintained at constant values for each experimental run.

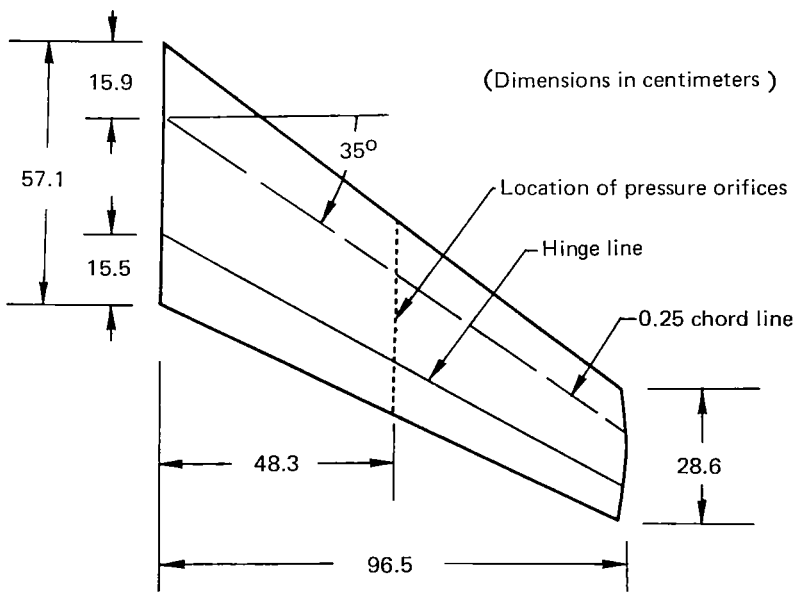

Figure 31.—Experimental Full-Span Flap Configuration of NACA RM A9G13

Experimental pressures were obtained along a streamwise section located at the 50% semispan station. The longitudinal junction between wing and flap was sealed to prevent leakage between the lower and upper surfaces at the hinge line.

The theoretical pressure distributions were obtained for modified boundary conditions that account for local streamwise velocity variations due to airfoil thickness effects. A comparison of the experimental and theoretical results is shown in figure 32.

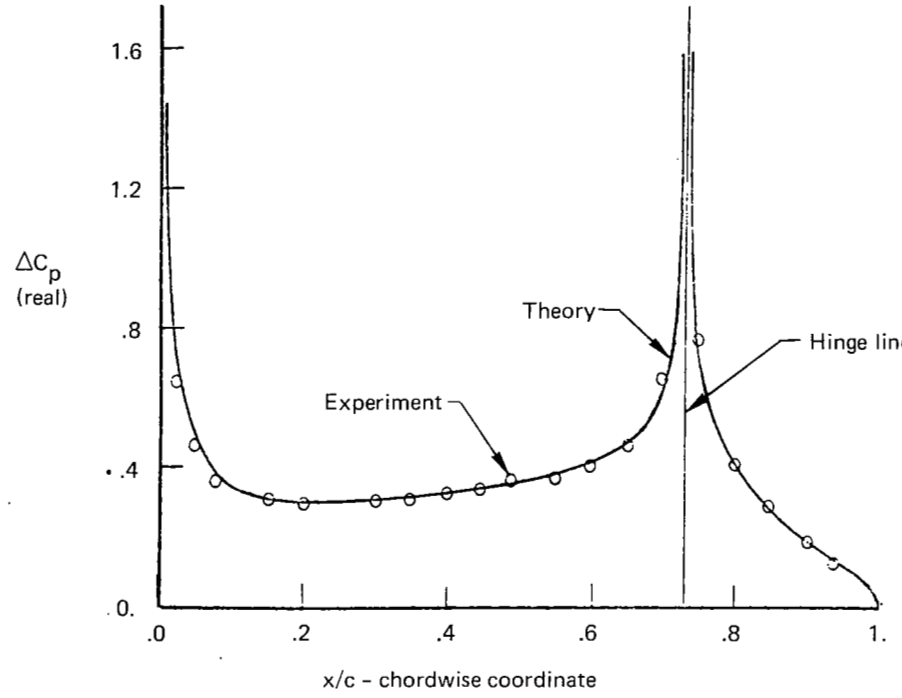

Figure 32.—Theoretical and Experimental Chordwise Pressure Distribution Obtained for a Full-Span Flap with $\delta = 10^o$, $\alpha = 0^o$, $M = 0.21$, $k = 0$

Since the sealed gap condition at the hinge line satisfies the theoretical assumptions (reference 3) a suitable basis is provided for evaluating the accuracy of the theoretical prediction. This comparison indicates that the experimental values are theoretically predicted within very close tolerances over the entire length of the chord, even in the vicinity of the hinge line.

Timing comparisons are shown in table 3 for two Mach number conditions. The results indicate that there is a small increase in relative computer cost with increasing Mach number.

Table 3.—Computer Timing Results for Steady-State Analysis of Full-Span Control Surface Configuration

			NASA CR-2543 (Sec.)	NASA CR-3009 (Sec.)	Ratio
	Total Execution Time		86.064	29.203	.3393
M = .21	Main surface C-Matrix	Total	5.842	2.301	.3939
		Per DWP	.243	.096	
	Control surface C-Matrix	Total	34.512	9.353	.2710
		Per DWP	1.438	.390	
M = .8	Main surface C-Matrix	Total	5.882	2.510	.4267
		Per DWP	.245	.105	
	Control surface C-Matrix	Total	34.513	9.671	.2802
		Per DWP	1.438	.403	

STEADY-STATE RESULTS FOR A PARTIAL-SPAN FLAP CONFIGURATION

The configuration with partial-span control surface, shown in figure 33, is taken from reference 8, representing a planform that was used in obtaining chordwise pressure distributions due to steady flap deflection. Pressures were obtained on a chordwise section located at the 46% semispan station. The hinge line gap was sealed, providing a suitable basis for comparing theoretical and experimental results.

The pressure comparison shown in figure 34 indicates that the experimental pressures are accurately predicted by the theoretical technique over a chordwise strip forward of the hinge line. The theoretical pressures on the control surface are only slightly larger than the experimental values. Consequently, it appears that the lifts and hinge moments may be predicted with reasonable accuracy for configurations having a sealed gap between wing and control surface.

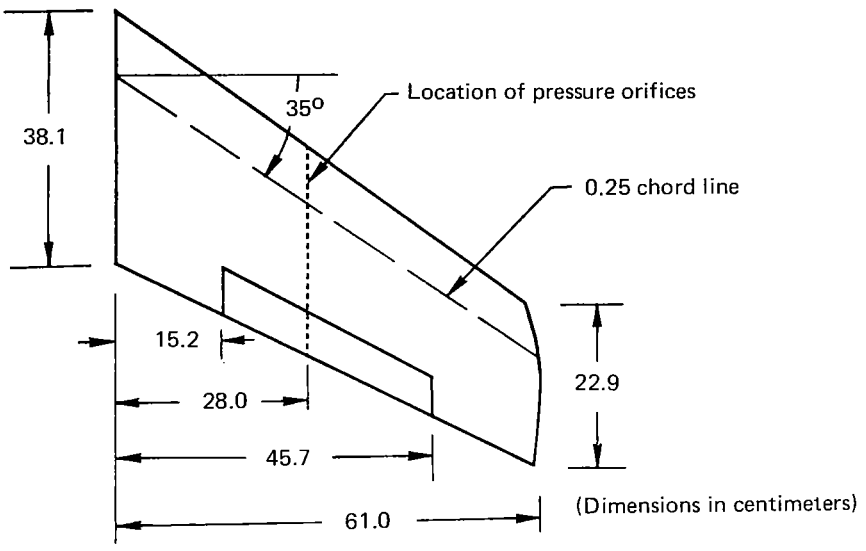

Figure 33.—Experimental Partial-Span Control Surface Configuration of NACA RM L53C23

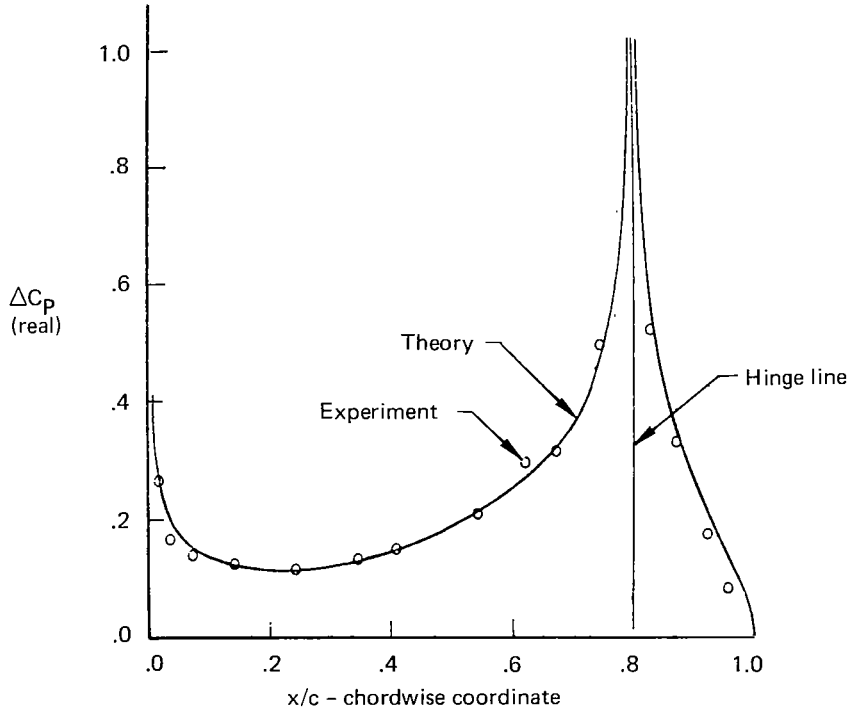

Figure 34.—Theoretical and Experimental Pressure Distribution for a Partial-Span Control Surface with $\delta = 10^{o}$, $\alpha = 0$, $M = 0.60$, $k = 0$

Table 4 provides a measure of the computer costs involved for the two Mach number cases for both the original and revised prediction technique.

Table 4.—Computer Timing Results for Steady-State Analysis of Partial-Span Control Surface Configuration

			NASA CR-2543 (Sec.)	NASA CR-3009 (Sec.)	Ratio
	Total Execution Time		102.525	37.431	.3651
M = .6	Main surface C-Matrix	Total	9.071	3.857	.4252
		Per DWP	.259	.110	
	Control surface C-Matrix	Total	38.337	10.654	.2770
		Per DWP	1.095	.304	
M = .8	Main surface C-Matrix	Total	8.978	3.974	.4426
		Per DWP	.257	.114	
	Control surface C-Matrix	Total	37.935	10.876	.2867
		Per DWP	1.084	.311	

SIDE-BY-SIDE CONTROL SURFACE CONFIGURATION

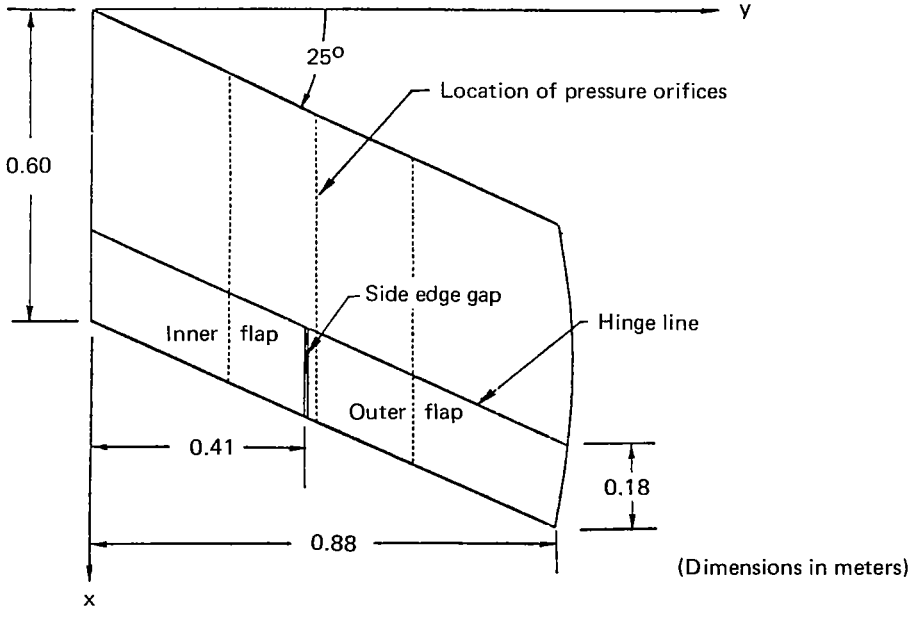

Figure 35.—Side-by-Side Control Surface Configuration

The side-by-side control surface configuration shown in figure 35 was used to obtain unsteady pressures for various combinations of flap deflections. The model has small open gaps at the hinge lines and side edges. Reference 6 provides no information on exact distances between control surface side edges and adjacent pressure measuring stations. The spanwise locations of experimental pressure chords were determined by measurement from the planform drawing.

Figures 36 and 37 present comparisons of theoretical and experimental pressures along a chord located near midspan of the oscillating control surface.

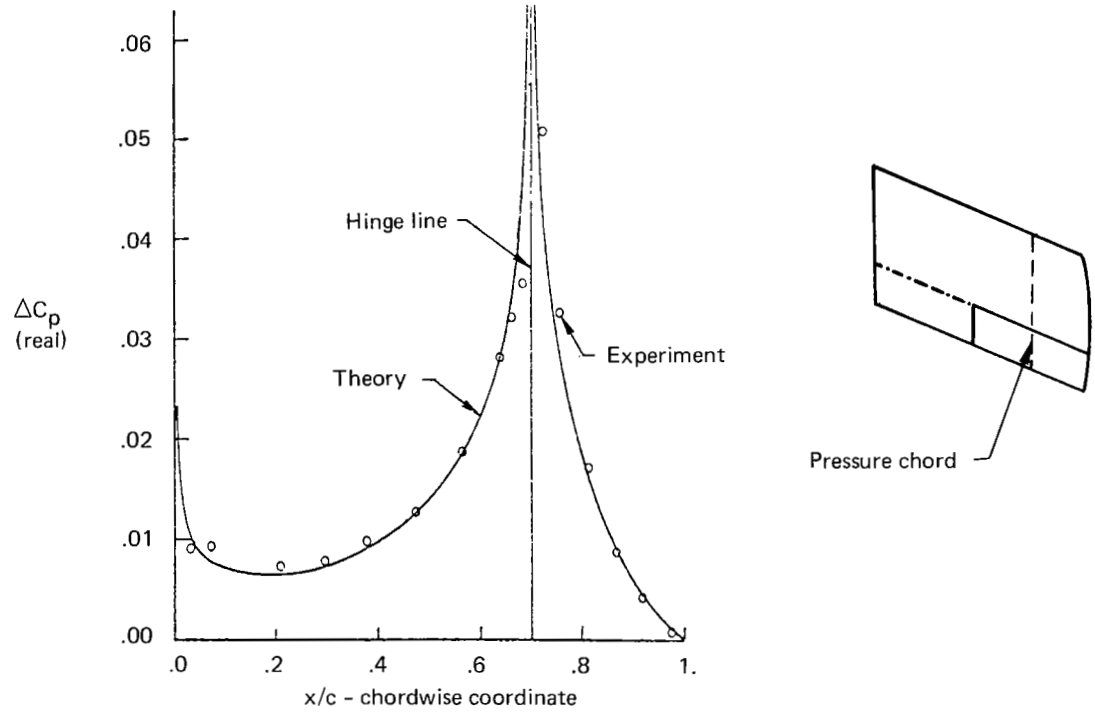

Figure 36.—In-Phase Part of the Chordwise Pressures Due to Motions of Outer Flap for a Pressure Chord Located on the Control Surface, M = 0, k = .372

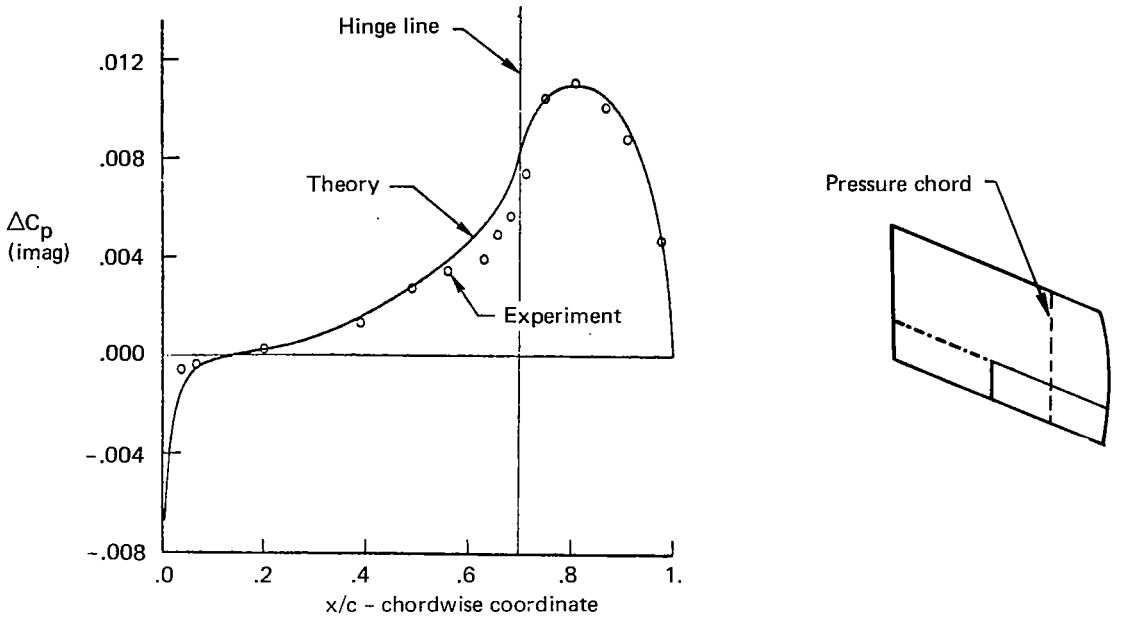

Figure 37.—Out-of-Phase Part of the Chordwise Pressures Due to Motions of Outer Flap for a Pressure Chord Located on the Control Surface, M = 0, k = .372

Figure 38 presents a comparison of pressures obtained at a station located far away from the oscillating control surface where the pressure magnitudes become quite small.

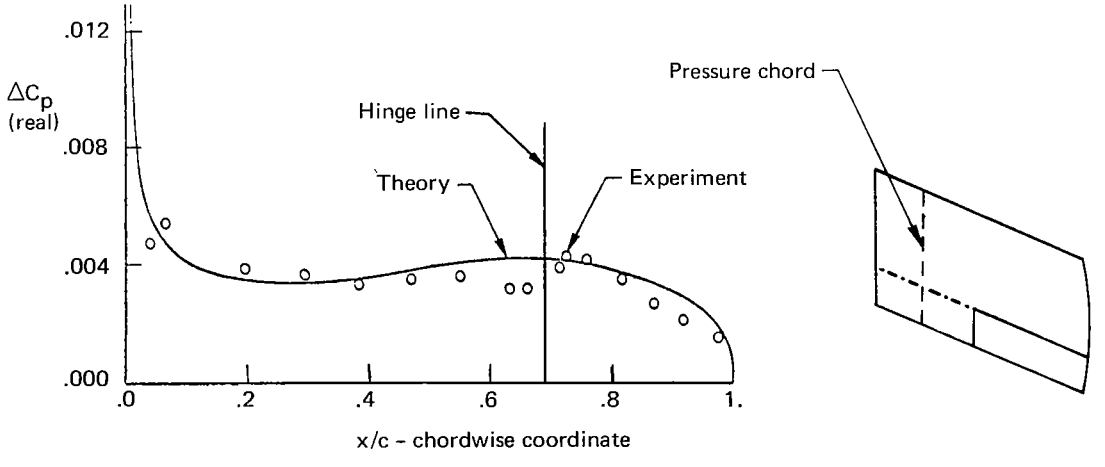

Figure 38.—In-Phase Part of Chordwise Pressures on a Chord Located at a Large Distance from the Control Surface

Table 5 presents timing comparisons indicating relative computer costs with six and nine downwash collocation chords.

Table 5.—Computer Timing Results Obtained in Analysis of the Side-by-Side Control Surface Configuration

			NASA CR-2543 (Sec.)	NASA CR-3009 (Sec.)	Ratio
	Total Execution Time		218.284	59.181	.2711
6 Collocation chords, 5 points per chord	Main surface C-Matrix	Total	17.481	8.510	.4868
		Per DWP	.583	.284	
	Inboard flap C-Matrix	Total	87.534	21.270	.2430
		Per DWP	2.918	.709	
	Outboard flap C-Matrix	Total	107.152	23.456	.2189
		Per DWP	3.572	.782	
9 Collocation chords, 5 points per chord	Total Execution Time		326.831	89.990	.2753
	Main surface C-Matrix	Total	26.421	15.376	.5820
		Per DWP	.587	.342	
	Inboard flap C-Matrix	Total	130.952	32.140	.2454
		Per DWP	2.910	.714	
	Outboard flap C-Matrix	Total	162.351	35.579	.2191
		Per DWP	3.608	.791	

SWEPT DELTA WING WITH LEADING AND TRAILING EDGE CONTROLS

The configuration shown in figure 39 is taken from reference 9, wherein experimental studies were reported on the use of active controls to suppress flutter. Steady state hinge moments obtained in this investigation were published in reference 10.

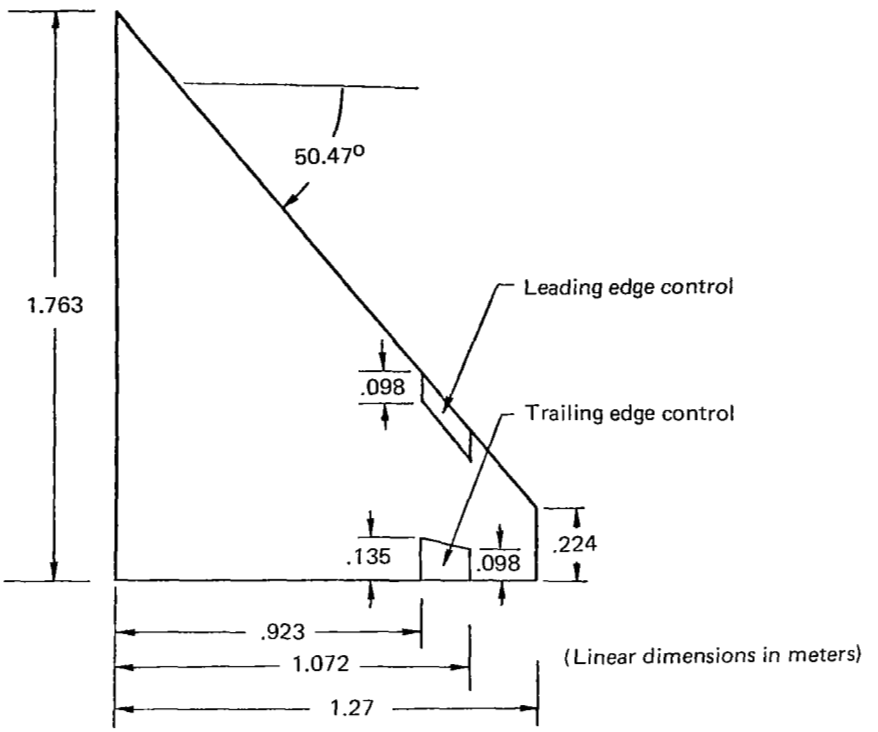

Figure 39.—Experimental Delta Wing Configuration of NASA TM X-2909

Figure 40 provides a comparison between theoretical and experimental hinge moments obtained for a leading edge and a trailing edge control surface deflection in steady flow.

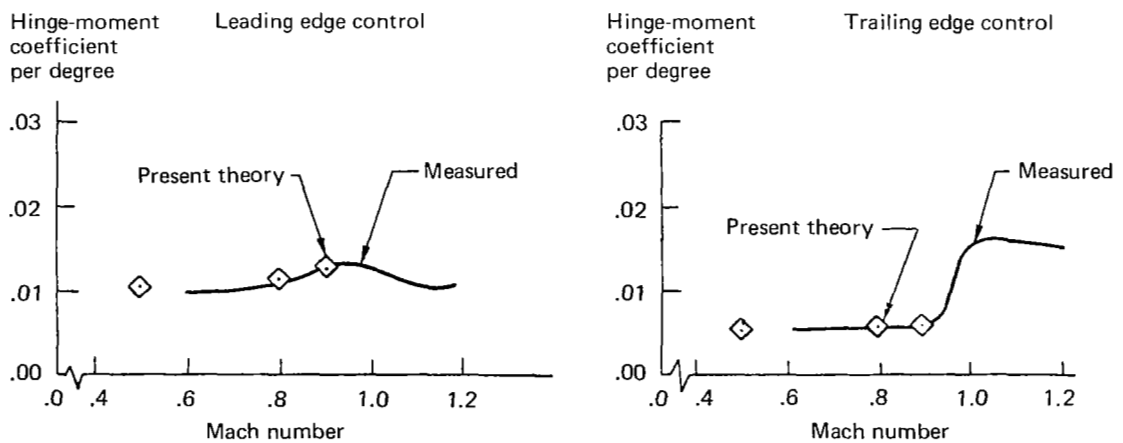

Figure 40.—Theoretical and Experimental Hinge-Moment Coefficients Obtained for Leading Edge and Trailing Edge Control Surfaces in Steady Flow

Table 6 provides a relative measure of the cost reductions that may now be achieved for predicting unsteady loadings caused by motions of leading edge control surfaces.

Table 6.—Computer Usage Timing Comparisons Obtained for an Oscillating Leading Edge Control Surface at M = .8, k = .5

		NASA CR-2543 (Sec.)	NASA CR-3009 (Sec.)	Ratio
Total Execution Time		777.161	134.640	.1732
Leading edge control surface C-Matrix	Total	495.574	60.356	.1218
	Per DWP	7.866	.958	
Trailing edge control surface C-Matrix	Total	228.373	38.034	.1665
	Per DWP	3.625	.604	
Main surface C-Matrix	Total	43.182	26.921	.6234
	Per DWP	.685	.427	

HIGH ASPECT RATIO TRANSPORT WING WITH CONTROLS

It should be noted that reasonable correlations obtained for the previous sample cases were achieved for configurations having large span control surfaces oscillating at small reduced frequencies. Numerical investigations conducted to evaluate solution convergence for small span control surfaces oscillating at high k values indicate that the number of analysis downwash chords needs to be increased in proportion to the k value and inversely proportional to the span length of the control surface.

Numerical investigations conducted to evaluate sensitivity in analysis of small span length control surfaces were accomplished using the wing and control surface configuration shown in figure 41. The 0.20 chord aileron has a 0.22 semispan and length and the 0.06 chord tab has a length of 0.12 semispan.

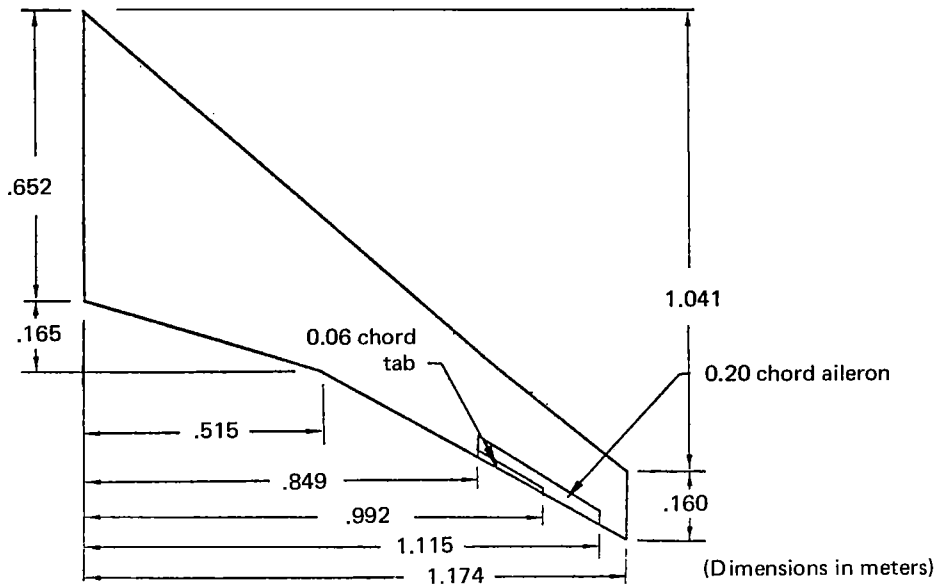

Figure 41.—Analysis Configuration Used to Evaluate Solution Sensitivity of Small Span Length Control Surface Configurations

Figure 42 presents a computer plot of the spanwise distribution of section lift due to aileron deflection in steady flow for two distributions of downwash chords in the analysis. The spanwise variation of the two lift distributions are almost identical. This indicates that converged and cost effective analyses may be achieved by using only a small number of downwash chords for steady flow analysis of small span control surfaces.

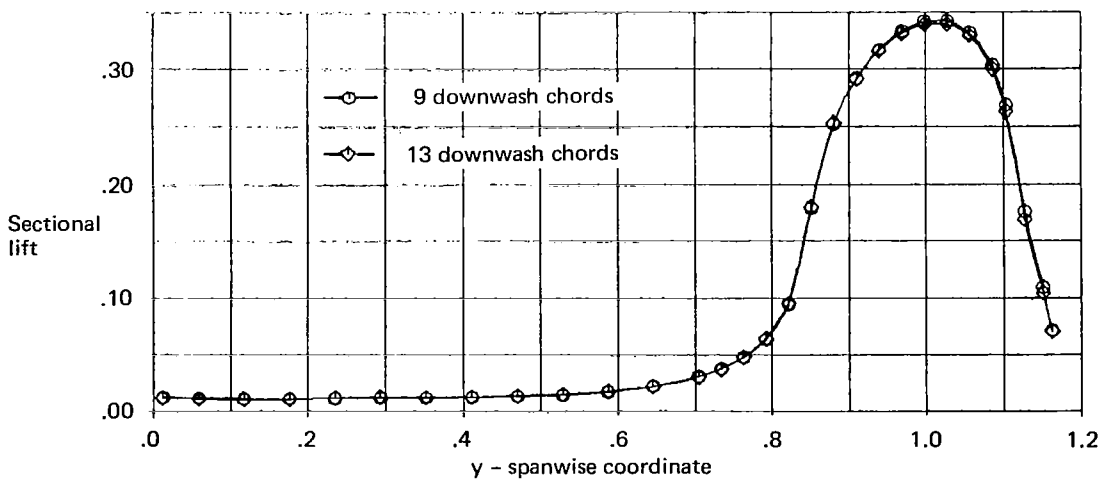

Figure 42.—Spanwise Lift Variation Due to Aileron Deflection in Steady Flow for Two Downwash Chord Distributions

Figure 43 presents the spanwise lift variation due to tab motions at k = 1.0, M = .8 for analyses with nine and thirteen downwash chords. The results indicate that the solutions are approaching convergence, but are not fully converged, even for the larger number of chords.

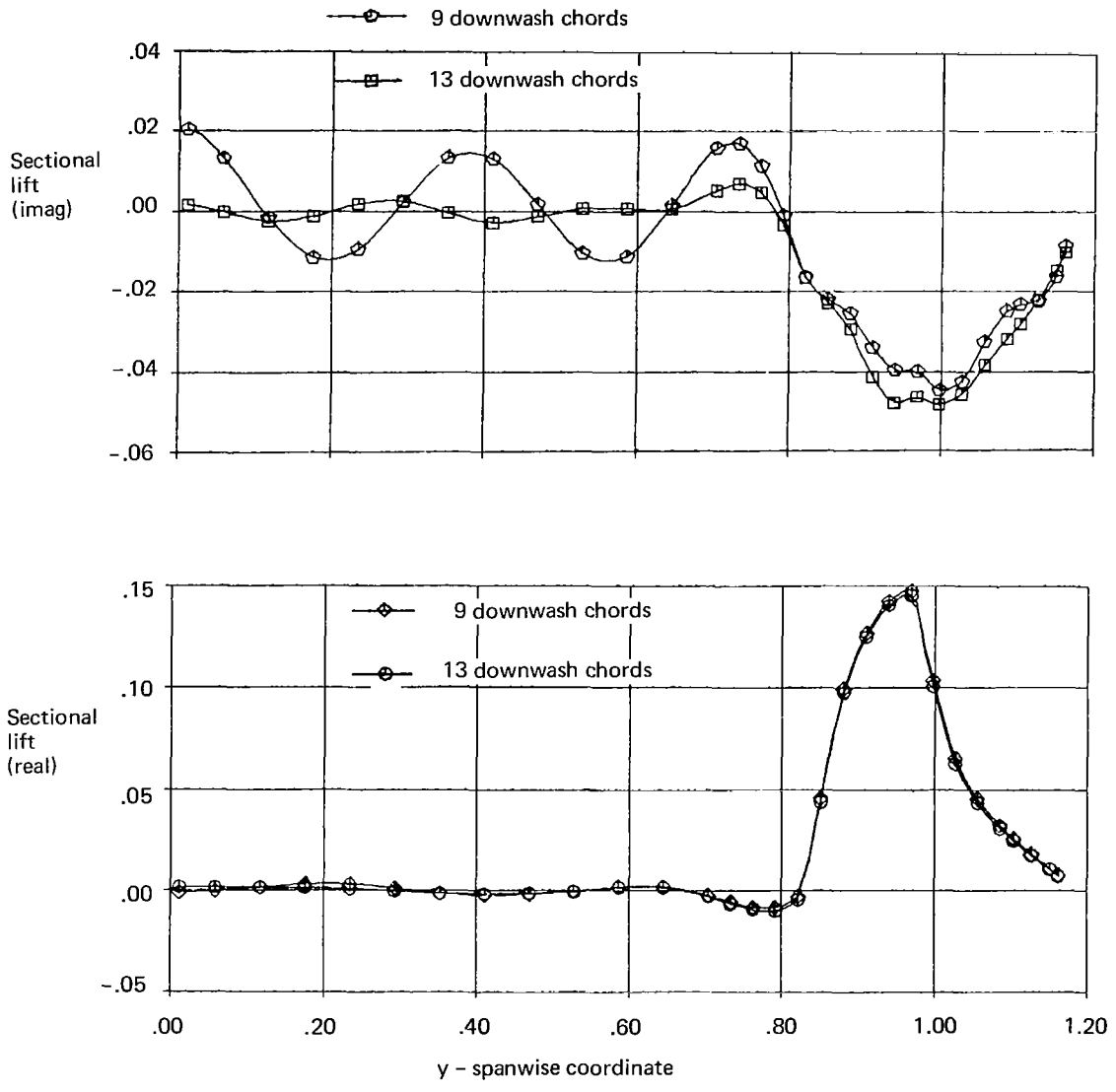

Figure 43.—Computer Plot of Spanwise Lift Variation Due to Tab Oscillation at k = 1.0, M = 0.8

Increasing the value of k tends to degrade the convergence for small span control surfaces, as shown in figure 44 for M = 0.8 and k = 2.0.

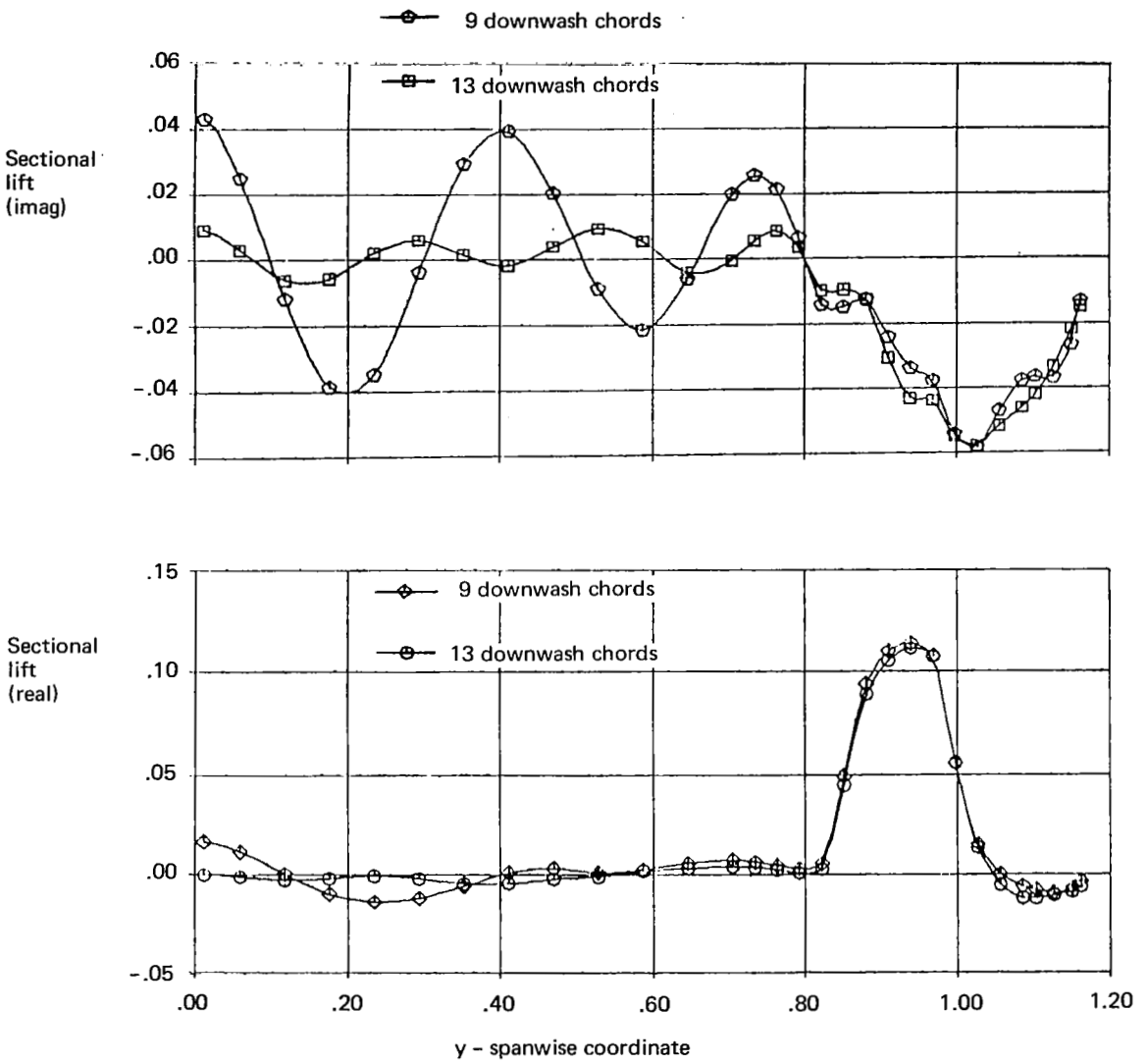

Figure 44.—Computer Plot of Spanwise Lift Variation Due to Tab Oscillation at k = 2.0, M = 0.8

Converged solutions may be obtained for small span control surface configurations, provided that sufficient care is taken in selecting the proper number of downwash chords to satisfy accuracy requirements.

Table 7 shows the relative reduction in computer costs obtained for this small span control surface analysis.

Table 7.–Computer Usage Timing Comparisons Obtained for Small Span Length Control Surface Analysis

				NASA CR-2543 (Sec.)	NASA CR-3009 (Sec.)	Ratio
13 collocation chords, 5 points per chord	k = 0	Total Execution Time		171.052	48.436	.2832
		Main surface C-Matrix	Total	17.234	10.033	.6402
			Per DWP	.265	.154	
		Aileron C-Matrix	Total	74.304	15.160	.2040
			Per DWP	1.143	.233	
		Tab C-Matrix	Total	70.761	14.444	.2041
			Per DWP	1.089	.222	
	k = 1	Total Execution Time		477.880	114.852	.2403
		Main surface C-Matrix	Total	39.720	30.598	.7703
			Per DWP	.611	.471	
		Aileron C-Matrix	Total	219.492	38.243	.1742
			Per DWP	3.377	.588	
		Tab C-Matrix	Total	208.891	36.683	.1756
			Per DWP	3.214	.564	
9 collocation chords, 5 points per chord	k = 0	Total Execution Time		119.180	32.736	.2747
		Main surface C-Matrix	Total	11.477	5.583	.4865
			Per DWP	.255	.124	
		Aileron C-Matrix	Total	51.901	10.396	.2003
			Per DWP	1.153	.231	
		Tab C-Matrix	Total	49.644	9.886	.1991
			Per DWP	1.103	.220	
	k = 1	Total Execution Time		333.484	78.491	.2354
		Main surface C-Matrix	Total	26.651	18.391	.6901
			Per DWP	.592	.409	
		Aileron C-Matrix	Total	152.173	27.221	.1789
			Per DWP	3.382	.605	
		Tab C-Matrix	Total	147.726	25.437	.1722
			Per DWP	3.283	.565	

CONCLUSIONS

Results of theoretical and numerical investigations to develop economical computing procedures have been applied to an existing computer program that predicts unsteady aerodynamic loadings caused by wing and control surface motions. Large reductions in computing costs were achieved by removing the spanwise singularity of the downwash integrand and evaluating its effect separately in closed form. Additional reductions were obtained by modifying the incremental pressure term that accounts for downwash singularities at control surface edges. Accuracy of theoretical predictions of unsteady loading at high reduced frequencies is increased by applying new pressure expressions that exactly satisfy the high frequency boundary conditions of an oscillating control surface. Comparative results indicate that the revised procedures provide more accurate predictions of unsteady loadings as well as reductions of 50 to 80 percent in computer usage costs.

APPENDIX A

DEVELOPMENT OF PRESSURE EXPRESSIONS THAT SATISFY THE BOUNDARY CONDITIONS OF A TRAILING EDGE CONTROL SURFACE HAVING A SWEPT HINGE LINE

Pressure expressions are formulated such that the change in boundary conditions are matched exactly around the edges of a trailing edge control surface. The analytical procedure used to obtain these expressions originates with the asymptotic expansion process suggested by Landahl in reference 3. Some of the symbols in this appendix are different from those in the main text and are defined where introduced.

The formulation of these pressure expressions follows the general procedure given NASA CR-2543. The present formulation differs from that of NASA CR-2543 in that the transformation previously used to eliminate the first order derivative term contained within the differential equation is no longer applied within this basic solution process.

The analysis coordinate system shown in figure 45 represents a segment of wing having a swept hinge line trailing edge control surface where local coordinates x, y are described in terms of ξ, η, x_c, y_s coordinates of figure 1. All coordinates are assumed to be nondimensionalized with respect to some reference length "ℓ."

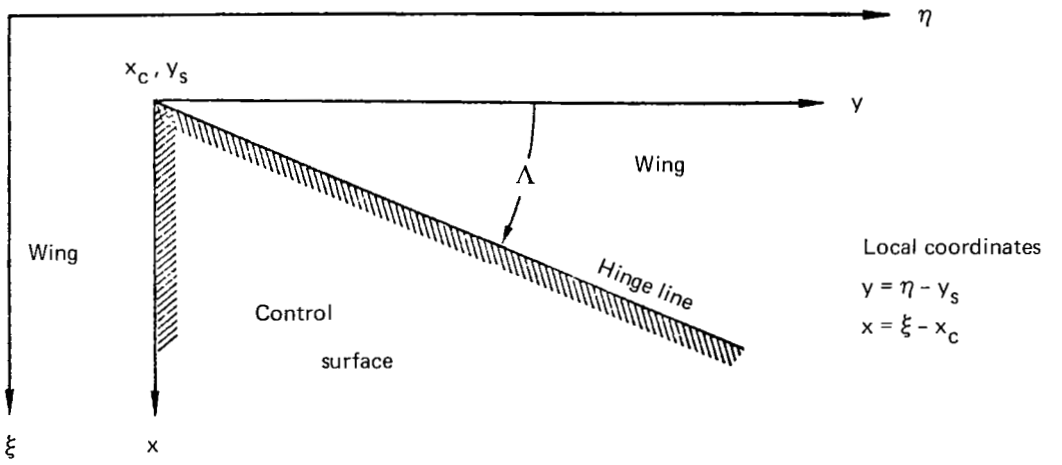

Figure 45.—Coordinate Definition for Analysis of Trailing Edge Controls

The linearized boundary value problem is developed in terms of the pressure perturbation coefficient $C_p = Pe^{ik\tau}$ where the pressure amplitude satisfies the differential equation of flow

$$\beta^2 P_{xx} + P_{yy} + P_{zz} - 2ikM^2 P_x + k^2 M^2 P = 0 \qquad \text{(A1)}$$

The motion of the system is defined as having the control surface oscillating about the hinge line and the rest of the wing is maintained in a stationary position.

The displacement Z_{cs} of the control surface is assumed to be simple harmonic and defined as:

$$\begin{aligned} Z_{cs} &= \Theta_H (x - x_c) e^{ik\tau} \\ &= \bar{Z}_{cs} e^{ik\tau} \end{aligned} \qquad \text{(A2)}$$

where $\tau = \frac{Vt}{\ell}$ nondimensional time.

The boundary conditions resulting from this motion are then given as:

$$P_z = -2\left[\frac{1}{\beta}\delta(x - x_c) + 2ikU(x - x_c) - k^2 (x - x_c) U(x - x_c)\right] U(y) \qquad \text{(A3)}$$

where the unit functions

$$U(x - x_c) = \begin{cases} 0 & x < x_c \\ 1 & x > x_c \end{cases}$$

$$U(y) = \begin{cases} 0 & y < 0 \\ 1 & y > 0 \end{cases}$$

and $\delta(\quad)$ is the Dirac delta function

The coordinates are scaled to remove the β^2 factor from the differential equation by letting $x = \beta x_0$, $y = y_0$, $z = z_0$ and using the relationship $x - x_c = x - y \tan \Lambda$

$$\begin{aligned} x - x_c &= x - y \tan \Lambda \\ &= \beta x_0 - \beta y_0 \frac{\tan \Lambda}{\beta} \\ &= \beta (x_0 - y_0 \tan \Lambda_1) \end{aligned}$$

The boundary value problem then takes on the definition of:

$$P_{x_0x_0} + P_{y_0y_0} + P_{z_0z_0} - \frac{2ikM^2}{\beta} P_{x_0} + k^2M^2P = 0$$

$$P_{\bar{z}_0} = -2\left[\frac{1}{\beta}\delta(x_0 - y_0\tan\Lambda_1) + 2ikU(x_0 - y_0\tan\Lambda_1) - k^2\beta(x_0 - y_0\tan\Lambda_1)U(x_0 - y_0\tan\Lambda_1)\right]U(y_0) \qquad \text{(A4)}$$

The coordinates are now scaled by the local scaling factor ϵ ($\epsilon << 1$) by letting

$$(x_0, y_0, z_0)_{old} = (\epsilon x_0, \epsilon y_0, \epsilon z_0)_{new} \qquad \text{(A5)}$$

and the amplitude of the pressure expression is expanded in a series in increasing powers of ϵ

$$P = P^0 + \epsilon P^1 + \epsilon^2 P^2 + \cdots \qquad \text{(A6)}$$

where the superscripts on ϵ are exponents, but the superscripts on P denote the order of the P function and are not exponents.

The new coordinate definitions of equation (A5) along with the expanded potential expression of equation (A6) are inserted into boundary value problem definition of equation (A4) to produce a series of new boundary value problems that are separated with respect to ϵ.

The set of boundary value problems resulting from this process are given as follows:

$$\left.\begin{aligned} &P^0_{x_0x_0} + P^0_{y_0y_0} + P^0_{z_0z_0} = 0 \\ &P^0_z = -2\theta_H\left[\frac{1}{\beta}\delta(x_0 - y_0\tan\Lambda_1)\right]U(y_0) \quad \text{on } z_0 = 0 \end{aligned}\right\} \quad \begin{matrix}\text{Zeroth} \\ \text{order, } \epsilon^0\end{matrix} \qquad \text{(A7)}$$

$$P^1_{x_0x_0} + P^1_{y_0y_0} + P^1_{z_0z_0} = \frac{2ikM^2}{\beta} P^0_{x_0}$$

$$P^1_{z_0} = -4\theta_H ik\, U(x_0 - y_0 \tan\Lambda_1)\, U(y_0) \quad \text{on } z_0 = 0$$

First order, ϵ^1 (A8)

$$P^2_{x_0x_0} + P^2_{y_0y_0} + P^2_{z_0z_0} = \frac{2ikM^2}{\beta} P^1_{x_0} - k^2M^2P^0$$

$$P^2_{z_0} = 2\theta_H k^2 \beta (x_0 - y_0 \tan\Lambda_1)\, U(x_0 - y_0 \tan\Lambda_1)\, U(y_0) \quad \text{on } z_0 = 0$$

Second order, ϵ^2 (A9)

$$P^3_{x_0x_0} + P^3_{y_0y_0} + P^3_{z_0z_0} = \frac{2ikM^2}{\beta} P^2_{x_0} - k^2M^2P^1$$

$$P^3_{z_0} = 0 \quad \text{on } z_0 = 0$$

Third order, ϵ^3 (A10)

$$P^n_{x_0x_0} + P^n_{y_0y_0} + P^n_{z_0z_0} = \frac{2ikM^2}{\beta} P^{n-1}_{x_0} - k^2M^2P^{n-2}$$

$$P^n_{z_0} = 0 \quad \text{on } z_0 = 0$$

N'th order, ϵ^n $(n \geq 3)$ (A11)

It is to be noted that solutions of the boundary value problems of the third order or greater do not contribute to a change in boundary conditions across the control surface boundaries but only contribute nonsingular pressures to the overall expression. Thus, solutions are required only for the boundary value problems defined equations (A7), (A8), and (A9).

The solution of equation (A7) for the zeroth order boundary value problem in unscaled coordinates is given by equation (A21) of NASA CR-2543 as:

$$P^0(x,y,0) = \frac{-\theta_H}{\pi\bar{\beta}} \ln\left[\sqrt{x^2+\beta^2y^2} - \left(\frac{\beta^2 y + x\tan\Lambda_1}{\bar{\beta}}\right)\right]$$

where

$$\left.\begin{aligned} x &= \xi - x_{c_s} \\ y &= \eta - y_s \\ \tan\Lambda_1 &= \frac{\tan\Lambda}{\beta} \\ \bar{\beta} &= \sqrt{\beta^2+\tan^2\Lambda} \end{aligned}\right\} \quad \text{unscaled coordinates} \qquad \text{(A12)}$$

now with scaled coordinates $x_0 = x/\beta\varepsilon$; $y_0 = y/\varepsilon$; $z_0 = z/\varepsilon$

the expression takes on the form:

$$P^0(x_0,y_0,0) = \frac{-\theta_H}{\pi\bar{\beta}} \ln\left[\sqrt{x_0^2+y_0^2} - (x_0\sin\Lambda_1 + y_0\cos\Lambda_1)\right] \qquad \text{(A13)}$$

It is now useful to make a rigid body rotation of coordinates defined by the following sketch:

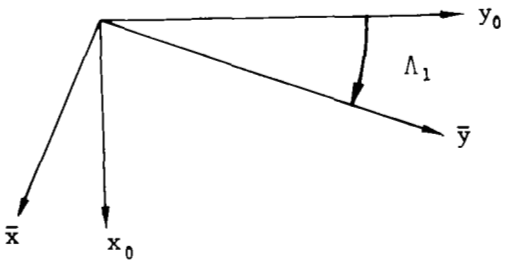

$$\left.\begin{aligned} \bar{x} &= x_0\cos\Lambda_1 - y_0\sin\Lambda_1 \\ \bar{y} &= x_0\sin\Lambda_1 + y_0\cos\Lambda_1 \\ \bar{z} &= z_0 \end{aligned}\right\} \qquad \text{(A14)}$$

then $$P^0 = -\frac{\theta_H}{\pi\bar{\beta}} \ln\left[r - \bar{y}\right]$$

where $$r = \sqrt{x_0^2+y_0^2} \equiv \sqrt{\bar{x}^2+\bar{y}^2}$$

The first order boundary value problem (equation (A8)) is restated here for convenience as:

$$\left.\begin{aligned} \nabla^2 P^1(x_0,y_0,z_0) &= \frac{2ikM^2}{\beta}\frac{\partial P^0(x_0,y_0,z_0)}{\partial x_0} \\ \frac{\partial P^1(x_0,y_0,z_0)}{\partial z_0} &= -4\theta_H ikU(x_0-y_0\tan\Lambda_1)U(y_0) \end{aligned}\right\} \qquad \text{(A15)}$$

The x_0 derivative expressed in rotated coordinates is

$$\frac{\partial}{\partial x_0} = \frac{\partial}{\partial \bar{x}}\frac{\partial \bar{x}}{\partial x_0} + \frac{\partial}{\partial \bar{y}}\frac{\partial \bar{y}}{\partial x_0} = \cos\Lambda_1 \frac{\partial}{\partial \bar{x}} + \sin\Lambda_1 \frac{\partial}{\partial \bar{y}}$$

$$= \frac{\beta}{\bar{\beta}}\frac{\partial}{\partial \bar{x}} + \frac{\tan\Lambda}{\beta}\frac{\partial}{\partial y}$$

where $\tan\Lambda_1 = \frac{\tan\Lambda}{\beta}$ and $\bar{\beta} = \sqrt{\beta^2 + \tan^2\Lambda}$

The boundary value problem of equation (A15) described in rotated coordinates is given as

$$\nabla^2 P^1(\bar{x},\bar{y},\bar{z}) = \frac{2ikM^2}{\bar{\beta}}\frac{\partial}{\partial \bar{x}}P^0(\bar{x},\bar{y},\bar{z}) + \frac{2ikM^2\tan\Lambda}{\beta\bar{\beta}}\frac{\partial}{\partial \bar{y}}P^0(\bar{x},\bar{y},\bar{z})$$

$$\frac{\partial P^1(\bar{x},\bar{y},\bar{z})}{\partial \bar{z}} = -4\theta_H ikU(\bar{x})U(\bar{y}-\bar{x}\tan\Lambda_1)$$

The above boundary value problem is then decomposed into three separate parts for ease of solution. The complete solution for $P^1(\bar{x},\bar{y},\bar{z})$ is obtained by summing the solutions of the three parts defined as

$$\left.\begin{aligned} \nabla^2 P^{11}(\bar{x},\bar{y},\bar{z}) &= \frac{2ikM^2}{\bar{\beta}}\frac{\partial P^0(\bar{x},\bar{y},\bar{z})}{\partial \bar{x}} \\ \left.\frac{\partial P^{11}}{\partial \bar{z}}\right|_{\bar{z}=0} &= 0 \end{aligned}\right\} \qquad \text{(A16)}$$

$$\left.\begin{aligned} \nabla^2 P^{12}(\bar{x},\bar{y},\bar{z}) &= \frac{2ikM^2\tan\Lambda}{\beta\bar{\beta}}\frac{\partial P^0(\bar{x},\bar{y},\bar{z})}{\partial \bar{y}} \\ \left.\frac{\partial P^{12}}{\partial \bar{z}}\right|_{\bar{z}=0} &= 0 \end{aligned}\right\} \qquad \text{(A17)}$$

$$\left.\begin{aligned} &\nabla^2 P^{13}(\bar{x},\bar{y},\bar{z}) = 0 \\ &\left.\frac{\partial P^{13}}{\partial \bar{z}}\right|_{\bar{z}=0} = -4\theta_H ikU(\bar{x})U(\bar{y}-\bar{x}\tan\Lambda_1) \end{aligned}\right\} \qquad \text{(A18)}$$

Solution of equation (A18) may be obtained by a straightforward application of Green's theorem and the solutions of equations (A16) and (A17) are obtained by applying flux theorem to these Poisson equations in the manner discussed by Hewitt in reference 5.

An example of the process used to obtain a solution of Poisson's equation is given as follows:

Consider equation (A16) rewritten as:

$$\left.\begin{aligned} &\nabla^2 P^1 = \frac{2ikM^2}{\bar{\beta}} P^0_{\bar{x}} \\ &P^1_{\bar{z}}\Big|_{\bar{z}=0} = 0 \end{aligned}\right\} \qquad \text{(A19)}$$

From equation (A13), the P^0 solution of the zeroth order boundary value problem is given in rotated coordinates as:

$$P^0 = -\frac{\theta_H}{\pi\bar{\beta}} \log(\bar{r}-\bar{y}) \qquad \text{A(20)}$$

where

$$\bar{r} = \sqrt{\bar{x}^2+\bar{y}^2+\bar{z}^2}$$

$$\bar{y} = x_0 \sin\Lambda_1 + y_0 \cos\Lambda$$

The first step is to take a derivative with respect to $\bar{y}$

$$P^0_{\bar{y}} = +\frac{\theta_H}{\pi\bar{\beta}} \left(\frac{1}{\bar{r}}\right)$$

then a derivative with respect to $\bar{x}$ is denoted as:

$$P^{\theta}_{\bar{x}\bar{y}} = + \frac{\theta_H}{\pi\bar{\beta}} \frac{\partial}{\partial\bar{x}}\left(\frac{1}{\bar{r}}\right)$$

The Poisson equation then becomes:

$$\nabla^2 P^1_{\bar{y}} = \frac{2ikM^2}{\bar{\beta}} \frac{\theta_H}{\pi\bar{\beta}} \frac{\partial}{\partial\bar{x}}\left(\frac{1}{\bar{r}}\right) \tag{A21}$$

From an extension of Green's theorem, the solution of a Poisson equation is given as:

$$P^1_{\bar{y}} = \frac{\theta_H}{\pi\bar{\beta}^2} \, 2ikM^2 \, \frac{-1}{4\pi} \iiint_V \frac{\partial}{\partial\bar{x}_1}\left(\frac{1}{\bar{r}_1}\right) \frac{d\bar{x}_1 \, d\bar{y}_1 \, d\bar{z}_1}{\bar{R}_1}$$

where

$$\bar{r}_1 = \sqrt{\bar{x}_1^2 + \bar{y}_1^2 + \bar{z}_1^2}$$

$$\bar{R}_1 = \sqrt{(\bar{x}_1 - \bar{x})^2 + (\bar{y}_1 - \bar{y})^2 + (\bar{z}_1 - \bar{z})^2}$$

and the volume V can occupy all space. Using the relationship of:

$$\frac{\partial}{\partial\bar{x}_1}\left(\frac{1}{\bar{R}_1}\right) = - \frac{\partial}{\partial x}\left(\frac{1}{\bar{R}_1}\right)$$

and performing an integration by parts gives the result:

$$P^1_y = \frac{\theta_H}{\pi\bar{\beta}^2} (2ikM^2) \frac{\partial J_1}{\partial x} \tag{A22}$$

where

$$J_1 = -\frac{1}{4\pi} \iiint_V \frac{1}{r_1} \frac{d\bar{x}_1 \, d\bar{y}_1 \, d\bar{z}_1}{\bar{R}_1}$$

and may be interpreted as the potential at the point $\bar{x}, \bar{y}, \bar{z}$ due to a distribution of sources of strength $1/r_1$. The potential J_1 is spherically symmetrical with respect to the origin, and the value of J_1 may be obtained by applying Gauss's flux theorem to a sphere of radius r that yields the relationship:

$$J_1(r) = \frac{r}{2} + \text{constant} \tag{A23}$$

Inserting equation (A23) into equation (A22) results in:

$$P^1_{\bar{y}} = \frac{\theta_H}{\pi\bar{\beta}^2} ikM^2 \frac{\bar{x}}{\bar{r}}$$

and the final solution obtained for P^1 is obtained by integrating with respect to $\bar{y}$ to yield:

$$P^1 = \frac{\theta_H}{\pi\bar{\beta}^2} ikM^2 \bar{x} \log(\bar{r}+\bar{y}) \tag{A24}$$

The solutions for the remaining components of the first order problem may be obtained in a similar manner and are summarized as follows:

$$\left.\begin{aligned}
&P^1 = P^{11}+P^{12}+P^{13} \\
&P^{11} = \frac{\theta_H}{\pi} \frac{ikM^2}{\bar{\beta}^2} \bar{x} \log(\bar{r}+\bar{y}) \\
&P^{12} = \frac{\theta_H}{\pi} \frac{ikM^2 \tan\Lambda}{\beta\beta^2} \sqrt{\bar{x}^2+\bar{y}^2+\bar{z}^2} \\
&P^{13} = \frac{\theta_H}{\pi}(-2ik)\, x \log(\bar{r}-\bar{y}) \\
&\quad + \frac{\theta_H}{\pi}(-2ik)\, y_0 \log(r_0-x_0)
\end{aligned}\right\} \tag{A25}$$

In like manner, the second order boundary value problem of equation (A9) is subdivided into components that are readily solved and the sum of the solutions will satisfy the second order boundary value problem of equation (A9).

The second order problem is restated here for convenience

$$\left.\begin{aligned} \nabla^2 P^2 &= \frac{2ikM^2}{\beta} P^1_{x_0} - k^2 M^2 P^0 \\ \left.\frac{\partial P^2}{\partial z_0}\right|_{z_0=0} &= 2\theta_H k^2 \beta (x_0 - y_0 \tan\Lambda_1) U(x_0 - y_0 \tan\Lambda_1) U(y_0) \end{aligned}\right\} \quad \text{(A26)}$$

P^0 and P^1 are expressed in terms of the rigid rotated coordinates $\bar{x}$ and $\bar{y}$ in equation (A20) and equation (A25), respectively.

The boundary value problem can be expressed in terms of the $\bar{x}, \bar{y}, \bar{z}$ coordinates by formulating the x_0 derivative in the rigid rotated coordinate system as

$$\frac{\partial}{\partial x_0} = \frac{\beta}{\bar{\beta}} \frac{\partial}{\partial \bar{x}} + \frac{\tan\Lambda}{\bar{\beta}} \frac{\partial}{\partial \bar{y}}$$

and applying the relationship between the Laplacians of rigid rotated coordinate systems given as

$$\nabla^2 P(x_0, y_0, z_0) \equiv \nabla^2 P(x, y, z)$$

The second order problem described in the rigid rotated coordinate system, $\bar{x}, \bar{y}, \bar{z}$ is then given as

$$\nabla^2 P^2(\bar{x}, \bar{y}, \bar{z}) = \frac{2ikM^2}{\bar{\beta}} \frac{\partial P(\bar{x}, \bar{y}, \bar{z})}{\partial \bar{x}} + \frac{2ikM^2 \tan\Lambda}{\beta\bar{\beta}} \frac{\partial P(\bar{x}, \bar{y}, \bar{z})}{\partial \bar{y}} - k^2 M^2 P^0$$

$$\left.\frac{\partial P^2(\bar{x}, \bar{y}, \bar{z})}{\partial \bar{z}}\right|_{\bar{z}=0} = 2\theta_H k^2 \bar{\beta}\, \bar{x}\, U(\bar{x}) U(\bar{y} - \bar{x} \tan\Lambda_1)$$

The boundary value problem is then decomposed into four separate parts for ease of solution. The solution $P^2(x, y, z)$ is obtained by summing P^{21}, P^{22}, P^{23}, and P^{24} that are solution results of the four separate boundary value problems defined as

$$\left.\begin{aligned} \nabla^2 P^{21}(\bar{x},\bar{y},\bar{z}) &= \frac{2ikM^2}{\bar{\beta}} \frac{\partial P^1(\bar{x},\bar{y},\bar{z})}{\partial x} \\ P^{21}_{\bar{z}}\Big|_{\bar{z}=0} &= 0 \end{aligned}\right\} \tag{A27}$$

$$\left.\begin{aligned} \nabla^2 P^{22}(\bar{x},\bar{y},\bar{z}) &= \frac{2ikM^2}{\beta\bar{\beta}} \tan\Lambda \frac{\partial P^1(\bar{x},\bar{y},\bar{z})}{\partial \bar{y}} \\ P^{22}_{\bar{z}}\Big|_{\bar{z}=0} &= 0 \end{aligned}\right\} \tag{A28}$$

$$\left.\begin{aligned} \nabla^2 P^{23}(\bar{x},\bar{y},\bar{z}) &= -k^2M^2P^0(\bar{x},\bar{y},\bar{z}) \\ P^{23}_{\bar{z}}\Big|_{\bar{z}=0} &= 0 \end{aligned}\right\} \tag{A29}$$

$$\left.\begin{aligned} \nabla^2 P^{24}(x_0,y_0,z_0) &= 0 \\ P^{24}_{z_0}\Big|_{z_0=0} &= 2\theta_H k^2 \beta (x_0 - y_0 \tan\Lambda_1) U(x_0 - y_0 \tan\Lambda_1) U(y_0) \end{aligned}\right\} \tag{A30}$$

Solutions of equations (A27) and (A28) are obtained for these Poisson equations in the manner previously described after the appropriate differentiation of equation (A25) has been accomplished. Also, equation (A29) may be solved in the manner previously described for this Poisson equation. The solution of equation (A30) is accomplished by a straightforward application of Green's theorem.

The solution of the second order boundary value problem is the sum of the solutions of the above boundary value problems, i.e.

$$P^2 = P^{21} + P^{22} + P^{23} + P^{24}$$

Thus, the final expression describing the pressure loadings that will satisfy the change in boundary conditions around the boundaries of a trailing edge control surface may be given in unscaled coordinates of figure 45 as follows:

$$P(x,y,0) = P^0(x,y,0) + \varepsilon P^1(x,y,0) + \varepsilon^2 P^2(x,y,0)$$

$$\begin{aligned} P(x,y,0) = \frac{\theta_H}{\pi}\Bigg\{\Bigg[-\frac{1}{\bar{\beta}} + \frac{k^2}{2\beta_H}\left(1+\frac{1}{2}\frac{M^2}{\bar{\beta}^2}\right)\left(1+3\frac{M^2}{\bar{\beta}^2}\right)(x-y\tan\Lambda)^2\Bigg] \\ - \frac{i2k}{\bar{\beta}}\left(1+\frac{1}{2}\frac{M^2}{\bar{\beta}^2}\right)(x-y\tan\Lambda)\Bigg\}\log\left[\sqrt{x^2+\beta^2y^2} - \frac{(\beta^2 y + x\tan\Lambda)}{\bar{\beta}}\right] \\ + \frac{\theta_H}{\pi}\Big\{k^2(x-y\tan\Lambda) - i2k\Big\}y\log\left[\sqrt{x^2+\beta^2y^2} - x\right] \\ + \frac{\theta_H}{\pi}\left\{\frac{k^2}{2}\right\}\tan\Lambda\ y^2\log\left[\sqrt{x^2+\beta^2y^2} - x\right] \end{aligned} \qquad \text{(A31)}$$

Equation (A31) is the complete expression for the pressure loadings required to satisfy the boundary conditions on a trailing edge oscillating control surface that is no longer restricted by frequency limitations. This equation needs to have special modification functions applied to it such that planform edge boundary conditions are satisfied. This is accomplished by using the E_1 and "H" functions described in NASA CR-2543.

APPENDIX B

DEVELOPMENT OF PRESSURE DISTRIBUTIONS THAT SATISFY THE BOUNDARY CONDITIONS ON SWEPT WING HAVING A LEADING EDGE CONTROL SURFACE

Pressure distributions are formulated in this section such that the boundary conditions over an oscillating wing control surface configuration are satisfied for the general reduced frequency case. Some of the symbols used here differ from those of the main text and are defined where introduced.

The formulation of these pressure expressions follow the general procedure given in NASA CR-2543. The fundamental difference between the derivations made in this section and that of NASA CR-2543 is that the "x" derivative is retained in the linearized differential equation of flow instead of transforming the differential equation into canonical form as indicated by equation (B7) of NASA CR-2543.

The procedure used to transform the differential equation into canonical form provided a relatively simple set of boundary value problems that could be solved with the aid of Fourier transforms. However, the transformation of the differential equation also requires a transformation of the associated boundary conditions. The transformed boundary conditions then contain an exponential function $\exp\left(\frac{ikM^2}{\beta}\left(x - x_{\ell s}\right)\right)$ which was expanded and approximated by retaining only a few terms of the series within the original development of NASA CR-2543. The effect of retaining only a few terms in the expanded exponential boundary condition limits the applicable range of reduced frequencies to relatively small values for analysis of high Mach number cases. The pressure expressions have been reformulated such that there is no longer a frequency limitation on the high Mach number analysis cases.

The analysis coordinate system shown in figure 46 represents a segment of a swept wing leading edge that has a control surface that oscillates about a hinge line located aft of the leading edge. All coordinates are assumed to be nondimensionalized with respect to some reference length "ℓ."

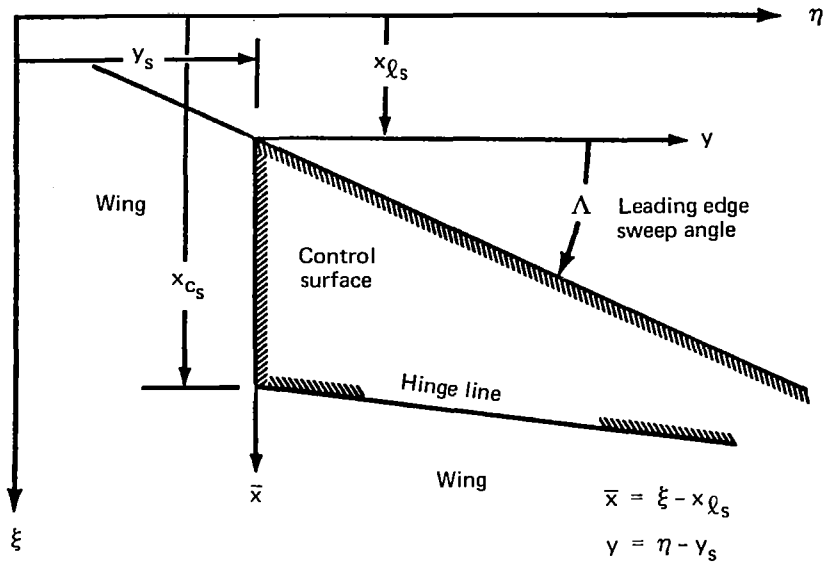

Figure 46.—Analysis Coordinate System

Solutions of the mixed boundary value problem are obtained from the linearized differential equation of flow given as

$$\beta^2 \phi_{\bar{x}\bar{x}} + \phi_{yy} + \phi_{zz} - 2ikM^2 \phi_{\bar{x}} + k^2 M^2 \phi = 0 \qquad \text{(B1)}$$

The motion of the system is defined as having the control surface oscillating about the hinge line and the rest of the wing is maintained in a stationary position.

The displacement Z_{CS} of the control surface is assumed to be simple harmonic and defined as

$$Z_{cs} = \theta_H (\bar{x} - \bar{x}_{cs}) e^{ik\tau} \qquad \text{(B2)}$$

$$= \bar{Z}_{cs} e^{ik\tau}$$

$$\tau = \frac{Vt}{\ell} \quad \text{(nondimensional time)}$$

The mixed boundary conditions are then defined as

$$\left.\begin{array}{lll} \left.\frac{\partial\phi}{\partial Z}\right|_{Z=0} = \frac{\partial Z_{cs}}{\partial \bar{x}} + ikZ_{cs} & y>0 & \\ \left.\frac{\partial\phi}{\partial Z}\right|_{Z=0} = 0 & y<0 & \text{Aft of Leading Edge} \\ \phi = 0 & & \text{Ahead of Leading Edge} \end{array}\right\} \quad \text{(B3)}$$

The "on-wing" boundary conditions may be combined using a unit function definition in "y"

$$U(y) = \begin{cases} 1 & y>0 \\ 0 & y<0 \end{cases}$$

The resulting boundary value problem is then defined as

$$\left.\begin{array}{lll} \beta^2\phi_{\bar{x}\bar{x}} + \phi_{yy} + \phi_{zz} - 2ikM^2\phi_{\bar{x}} + k^2M^2\phi = 0 & & \\ \phi_z = \theta_H\left[(1-ik\bar{x}_{cs}) + ik\bar{x}\right]U(y) & \bar{x}>y\tan\Lambda \text{ on } z=0 & \\ \phi = 0 \quad \text{on } z=0 & \bar{x}<y\tan\Lambda & \end{array}\right\} \quad \text{(B4)}$$

A transformation or coordinate scaling is made in order to simplify the differential equation by setting

$$x_0 = \bar{x}/\beta; \qquad y_0 = y; \qquad z_0 = z$$

This coordinate scaling results in a transformation of the leading edge definition as given by

$$x_0\beta = y_0\tan\Lambda$$

$$x_0 = y_0\tan\Lambda/\beta$$

$$= y_0\tan\Lambda_1$$

The new definition of the mixed boundary value problem is then described as

$$\left.\begin{aligned}
&\phi_{x_0x_0} + \phi_{y_0y_0} + \phi_{z_0z_0} - \frac{2ikm^2\phi}{\beta} x_0 + k^2M^2\phi = 0 \\
&\phi_{z_0} = (\lambda+\nu x_0)U(y_0) \qquad x_0 > y_0 \tan\Lambda_1 \quad \text{on } z_0 = 0 \\
&\phi = 0 \qquad\qquad\qquad\qquad x_0 < y_0 \tan\Lambda_1 \quad \text{on } z_0 = 0 \\
&\lambda = \theta_H(1-ikx_0); \qquad \nu = \theta_H(ik\beta)
\end{aligned}\right\} \qquad \text{(B5)}$$

In order to study the problem in the vicinity of the leading edge corner, all coordinates are stretched such that

$$(x_0, y_0, z_0)_{old} \longrightarrow (\varepsilon x_0, \varepsilon y_0, \varepsilon z_0)_{new}$$

The potential function is then expanded in a series given as

$$\phi = \phi^0 + \varepsilon^1\phi^1 + \varepsilon^2\phi^2 + \cdots$$

where the superscripts on ϵ are exponents, but the superscripts on ϕ denote the order of the ϕ function and are not exponents.

The expanded potential function is then inserted into the differential equation and associated boundary conditions of equation (B5). A series of new boundary value problems are obtained by collecting terms with respect to the powers of ϵ. The resulting set of boundary value problems are less complicated and may be solved more readily than attempting to solve the original boundary value problem of equation (B5).

The set of simplified boundary value problems resulting from the asymptotic expansion process are given as follows:

$$\left.\begin{aligned} &\nabla^2\phi^0 = 0 \\ &\phi^0_{z_0} = 0 \qquad \text{on } z=0; \quad x_0 > y_0\tan\Lambda_1 \\ &\phi^0 = 0 \qquad \text{on } z=0; \quad x_0 < y_0\tan\Lambda_1 \end{aligned}\right\} \quad \text{Zeroth order, } \epsilon^0 \qquad \text{(B6)}$$

$$\left.\begin{aligned} &\nabla^2\phi^1 = \frac{2ikM^2}{\beta}\phi^0_{x_0} \\ &\phi^1_{z_0} = \lambda\, U(y_0) \qquad \text{on } z=0; \quad x_0 > y_0\tan\Lambda_1 \\ &\phi^1 = 0 \qquad \text{on } z=0; \quad x_0 < y_0\tan\Lambda_1 \end{aligned}\right\} \quad \text{First order, } \epsilon^1 \qquad \text{(B7)}$$

$$\left.\begin{aligned} &\nabla^2\phi^2 = \frac{2ikM^2}{\beta}\phi^1_{x_0} - k^2M^2\phi^0 \\ &\phi^2_{z_0} = \nu x_0 U(y_0) \qquad \text{on } z=0; \quad x_0 > y_0\tan\Lambda_1 \\ &\phi^2 = 0 \qquad \text{on } z=0; \quad x_0 < y_0\tan\Lambda_1 \end{aligned}\right\} \quad \text{Second order, } \epsilon^2 \qquad \text{(B8)}$$

$$\left.\begin{aligned} &\nabla^2\phi^3 = \frac{2ikM^2}{\beta}\phi^2_{x_0} - k^2M^2\phi^1 \\ &\phi^3_{z_0} = 0 \qquad \text{on } z=0; \quad x_0 > y_0\tan\Lambda_1 \\ &\phi^3 = 0 \qquad \text{on } z=0; \quad x_0 < y_0\tan\Lambda_1 \end{aligned}\right\} \quad \text{Third order, } \epsilon^3 \qquad \text{(B9)}$$

$$\left.\begin{aligned} &\nabla^2\phi^n = \frac{2ikM^2}{\beta}\phi^{n-1}_{x_0} - k^2M^2\phi^{n-2} \\ &\phi^n_{z_0} = 0 \qquad \text{on } z=0; \quad x_0 > y_0\tan\Lambda_1 \\ &\phi^n = 0 \qquad \text{on } z=0; \quad x_0 < y_0\tan\Lambda_1 \end{aligned}\right\} \quad \text{N'th order, } \epsilon^n \ (n \geq 3) \qquad \text{(B10)}$$

The zeroth order boundary value problem may be solved in terms of an unknown coefficient multiplier that depends on the result of the global integration. However, the coefficient multiplier cannot be evaluated as a function of local boundary conditions only. Also, the boundary conditions across the side edge indicate that the resulting solution will be regular and not contribute to evaluating the finite change in boundary conditions. Consequently, the zeroth order solution will be omitted from this initial solution process. However, its effect will ultimately be included within the complete solution during the global integration that is performed at the end of the solution process which evaluates the final loadings using the generated residual downwashes as boundary conditions.

It should be noted that the third and higher order boundary value problems do not define a change in boundary conditions across the side edge of the control surface. As a result, the solutions of these problems provide continuous downwash distributions across the wing control surface boundaries which result in additional smoothness within the residual downwash sheets. However, experience has shown that only the boundary value problems that contain a discontinuity across the side edges in the boundary condition definition need to be considered in order to obtain reasonably smooth downwash sheets provided that not too high values of reduced frequency are applied within the analysis. Consequently, the third and subsequent boundary value problems are omitted from the solution process.

Thus, the critical boundary value problems to be solved are the first and second order problems as given by equations (B7) and (B8) with the ϕ^0 and $\phi^0_{x_0}$ terms set to zero. The sum of the solutions of these boundary value problems will then provide a means to exactly match the change in boundary conditions across the side edges of a leading edge control surface without having a frequency limitation that was previously implied within the development of NASA CR-2543.

The critical boundary value problems to be solved are then defined as

$$\left.\begin{aligned} &\nabla^2\phi^1 = 0 \\ &\phi^1_{z_0} = \lambda U(y_0) \quad \text{on } z=0; \quad x_0 > y_0 \tan\Lambda_1 \\ &\phi^1 = 0 \quad \text{on } z=0; \quad x_0 < y_0 \tan\Lambda_1 \end{aligned}\right\} \text{First order} \qquad \text{(B11)}$$

$$\left.\begin{aligned} &\nabla^2\phi^2 = \frac{2ikM^2}{\beta}\phi^1_{x_0} \\ &\phi^2_{z_0} = \nu x_0 U(y_0) \quad \text{on } z=0; \quad x_0 > y_0 \tan\Lambda_1 \\ &\phi^2 = 0 \quad \text{on } z=0; \quad x_0 < y_0 \tan\Lambda_1 \end{aligned}\right\} \text{Second order} \qquad \text{(B12)}$$

Solution of the first order boundary value problem has been obtained in NASA CR-2543 and its contribution to the pressure coefficient will be included at the end of this section.

The second order boundary value problem of equation (B8) has the form of a Poisson equation that complicates the solution process if it is retained in its present form. However, the differential equation may be changed into a more amenable form by applying a transformation to the definition of ϕ^2 such that

$$\phi^2 = \frac{ikM^2}{\beta} x_0 \phi^1 + \overline{\phi} \tag{B13}$$

where the form of $\overline{\phi}$ is to be determined. That is, ϕ^2 is defined as being a linear combination of ϕ^1 and a new function $\overline{\phi}$ as is implied from the form of the differential equation of equation (B8). The conditions imposed on ϕ^2 by ϕ^1 are known from the solution of the first order boundary value problem and it only remains to determine the conditions on $\overline{\phi}$ such that the linear combination provides a valid solution of the second order boundary value problem.

The coordinate subscripts are removed from the following discussion and will be replaced at the end of the derivation.

Restating the transformation

$$\phi^2 = \frac{ikM^2}{\beta} x\phi^1 + \overline{\phi}$$

then

$$\nabla^2\phi^2 = \frac{ikM^2}{\beta} \nabla^2(x\phi^1) + \nabla^2\overline{\phi}$$

and

$$\nabla^2(x\phi^1) = \frac{\partial^2}{\partial x^2}(x\phi^1) + x\left(\frac{\partial^2}{\partial y^2}+\frac{\partial^2}{\partial z^2}\right)\phi^1$$

$$= \frac{\partial}{\partial x}(x\phi^1_x + \phi^1) + x\left(\frac{\partial^2}{\partial y^2} + \frac{\partial^2}{\partial z^2}\right)\phi^1$$

$$= 2\phi^1_x + x\left(\frac{\partial^2}{\partial x^2} + \frac{\partial^2}{\partial y^2} + \frac{\partial^2}{\partial z^2}\right)\phi^1$$

$$= 2\phi^1_x + x\nabla^2\phi^1$$

Since $\nabla^2\phi^1 = 0$ from the definition of the first order boundary value problem, it follows that

$$\nabla^2\phi^2 = \frac{2ikM^2}{\beta}\phi^1_x + \nabla^2\overline{\phi}$$

From the definition of the boundary condition imposed on ϕ^2 within equation (B12), it follows that

$$\phi^2_z = \frac{ikM^2}{\beta} x\phi^1_z + \bar{\phi}_z = \frac{ikM^2}{\beta} x\lambda U(y) + \bar{\phi}_z \equiv \nu x U(y)$$

$$\text{on } z=0; \quad x > y\tan\Lambda_1$$

and

$$\phi^2 = \frac{ikM^2}{\beta} x\phi^1 + \bar{\phi} = \bar{\phi} \equiv 0 \qquad \text{for } x < y\tan\Lambda_1$$

Therefore, the conditions imposed on $\bar{\phi}$ are then defined as

$$\left.\begin{aligned} &\nabla^2\bar{\phi}=0 \\ &\bar{\phi}_z = (\nu - \frac{ikM^2}{\beta}\lambda) x U(y) \qquad \text{on } z=0; \quad x > y\tan\Lambda_1 \\ &\bar{\phi}=0 \qquad\qquad\qquad\qquad\qquad\qquad x < y\tan\Lambda_1 \end{aligned}\right\} \qquad \text{(B14)}$$

Thus, the solution of the second order boundary value problem of equation (B12) is given as

$$\phi^2 = \frac{ikM^2}{\beta} x\phi^1 + \text{the solution of equation (B14)}$$

It should be noted that solutions of ϕ^1 and $\bar{\phi}$ (of equation (B14)) have been obtained in NASA CR-2543. However, the pressure expressions resulting from the above are different from the expressions of NASA CR-2543 due to the transformation used in obtaining ϕ^2.

The new definition of the pressure loading functions are formulated using the expanded form of the potential function

$$\begin{aligned} \phi &= \varepsilon\phi^1 + \varepsilon^2\phi^2 \\ &= \varepsilon\phi^1 + \varepsilon^2\left(\frac{ikM^2}{\beta} x_0\phi^1 + \bar{\phi}\right) \end{aligned} \qquad \text{(B15)}$$

By definition, the loading functions written in terms of the pressure coefficients are given in unscaled coordinates as

$$C_p(\bar{x}, y, 0) = -2\left(\phi_{\bar{x}} + ik\phi\right) \qquad \text{(B16)}$$

Inserting equation (B15) into equation (B16) and performing the indicated operations results in the expression of the pressure coefficient that is valid for the general reduced frequency case

$$C_p(\bar{x}, y, 0) = -2\left[\left(1+\frac{ikM^2}{\beta^2}\bar{x}\right)\epsilon\phi^1_{\bar{x}} + \left(\frac{ik}{\beta^2}-\frac{k^2M^2}{\beta^2}\bar{x}\right)\epsilon\phi^1\right] \qquad (B17)$$
$$-2\left[\epsilon^2\bar{\phi}_{\bar{x}}+ik\epsilon^2\bar{\phi}\right]$$

From equation (B65) of NASA CR-2543, $\epsilon\phi^1$ is given in unscaled coordinates as

$$\epsilon\phi^1 = \frac{-2\lambda}{\pi}\mathrm{Im}\left\{\frac{i}{(i\beta+\tan\Lambda)}\,\bar{v}_0\bar{v}_1+\frac{iy}{2}\log\left[\frac{\bar{v}_0+\bar{v}_1}{\bar{v}_0-\bar{v}_1}\right]\right\} \qquad (B18)$$

where

$$\bar{v}_0 = \sqrt{\bar{x}+i\beta y}$$

$$\bar{v}_1 = \sqrt{\bar{x}-y\tan\Lambda}$$

The x derivative of $\epsilon\phi^1$ is obtained by noting that

$$\frac{\partial\bar{v}_0}{\partial\bar{x}} = \frac{1}{2\bar{v}_0}; \quad \frac{\partial\bar{v}_1}{\partial\bar{x}} = \frac{1}{2\bar{v}_1}; \quad \frac{\partial}{\partial\bar{x}}\left[\log\left(\frac{\bar{v}_0+\bar{v}_1}{\bar{v}_0-\bar{v}_1}\right)\right] = \frac{1}{\bar{v}_0\bar{v}_1}$$

$$y = (\bar{v}_0^2-\bar{v}_1^2)/(i\beta+\tan\Lambda) \text{ with } \bar{v}_1 \text{ being Real.}$$

Thus

$$\epsilon\phi^1_{\bar{x}} = \frac{-2\lambda}{\pi}\,\mathrm{Im}\left\{\frac{i}{(i\beta+\tan\Lambda)}\left(\frac{\bar{v}_0}{2\bar{v}_1}+\frac{\bar{v}_1}{2\bar{v}_0}\right)+\frac{iy}{2}\,\frac{1}{\bar{v}_0\bar{v}_1}\right\}$$

or (B19)

$$\epsilon\phi^1_{\bar{x}} = \frac{-2\lambda}{\pi\bar{\beta}^2\bar{v}_1}\mathrm{Im}\left\{(\beta+i\tan\Lambda)\sqrt{\bar{x}+i\beta y}\right\}$$

where

$$\bar{\beta}^2 = \beta^2+\tan^2\Lambda$$

The first part of the pressure coefficient of equation (B17) (that part involving ϕ^1) can then be written as

$$C_p^1(\bar{x},y,0)=-2\left\{\left(1+\frac{ikM^2}{\beta}\bar{x}\right)\varepsilon\phi^1_{\bar{x}}+\left(\frac{ik}{\beta^2}-\frac{k^2M^2}{\beta^2}\bar{x}\right)\varepsilon\phi^1\right\}$$

$$C_p^1(\bar{x},y,0)=-2\left\{\left(1+\frac{ikM^2}{\beta}\bar{x}\right)\left(\frac{-2\lambda}{\pi\bar{v}_1\bar{\beta}^2}\right)\mathrm{Im}\left[(\beta+i\tan\Lambda)\sqrt{\bar{x}+i\beta y}\right]\right. \qquad \text{(B20)}$$

$$\left.+\left(\frac{ik}{\beta^2}-\frac{k^2M^2}{\beta^2}\bar{x}\right)\mathrm{Im}\left[\left(\frac{-2\lambda}{\pi}\right)\bar{v}_0\bar{v}_1+\frac{iy}{2}\log\left[\frac{\bar{v}_0+\bar{v}_1}{\bar{v}_0-\bar{v}_1}\right]\right]\right\}$$

It can be shown that

$$\mathrm{Im}\left[(\beta+i\tan\Lambda)\bar{v}_0\right]=\frac{\beta\,\mathrm{Sgn}(y)}{\sqrt{2}}\sqrt{\sqrt{\bar{x}^2+\beta^2y^2}-\bar{x}}+\frac{\tan\Lambda}{\sqrt{2}}\sqrt{\sqrt{\bar{x}^2+\beta^2y^2}+\bar{x}}$$

$$\mathrm{Im}\left[i\log\left(\frac{\bar{v}_0+\bar{v}_1}{\bar{v}_0-\bar{v}_1}\right)\right]=\mathrm{Re}\left[\log\left(\frac{\bar{v}_0+\bar{v}_1}{\bar{v}_0-\bar{v}_1}\right)\right]$$

$$\mathrm{Re}\left[\log\left(\frac{\bar{v}_0+\bar{v}_1}{\bar{v}_0-\bar{v}_1}\right)\right]=$$

$$=\tfrac{1}{2}\log\left\{\frac{\sqrt{\bar{x}^2+\beta^2y^2}+(\bar{x}-y\tan\Lambda)+\sqrt{2}\sqrt{\bar{x}-y\tan\Lambda}\sqrt{\sqrt{\bar{x}^2+\beta^2y^2}+\bar{x}}}{\sqrt{\bar{x}^2+\beta^2y^2}+(\bar{x}-y\tan\Lambda)-\sqrt{2}\sqrt{\bar{x}-y\tan\Lambda}\sqrt{\sqrt{\bar{x}^2+\beta^2y^2}+\bar{x}}}\right\}$$

Inserting the above into equation (B20) and collecting terms results in a partial expression of the pressure coefficient of equation (B17) given as

$$C_p^1=-2\left[\left(1+\frac{ikM^2}{\beta^2}\bar{x}\right)\varepsilon\phi^1_{\bar{x}}+\left(\frac{ik}{\beta^2}-\frac{k^2M^2}{\beta^2}\bar{x}\right)\varepsilon\phi^1\right]$$

or

$$C_p^1=\frac{\lambda}{\pi}\left\{\frac{2\sqrt{2}}{\bar{\beta}^2}\left[\left(1+\frac{ikM^2}{\beta^2}\bar{x}\right)\Big/\sqrt{\bar{x}-y\tan\Lambda}+\left(\frac{ik}{\beta^2}-\frac{k^2M^2}{\beta^2}\bar{x}\right)\sqrt{\bar{x}-y\tan\Lambda}\right]\right.$$

$$\left[\beta\,\mathrm{Sgn}(y)\sqrt{\sqrt{\bar{x}^2+\beta^2y^2}-\bar{x}}+\tan\Lambda\sqrt{\sqrt{\bar{x}^2+\beta^2y^2}+\bar{x}}\right] \qquad \text{(B21)}$$

$$\left.+\left(\frac{ik}{\beta^2}-\frac{k^2M^2}{\beta^2}\bar{x}\right)y\log\left[\frac{\sqrt{\bar{x}^2+\beta^2y^2}+(\bar{x}-y\tan\Lambda)+\sqrt{2}\sqrt{\bar{x}-y\tan\Lambda}\sqrt{\sqrt{x^2+\beta^2y^2}+\bar{x}}}{\sqrt{\bar{x}^2+\beta^2y^2}+(\bar{x}-y\tan\Lambda)+\sqrt{2}\sqrt{\bar{x}-y\tan\Lambda}\sqrt{\sqrt{\bar{x}^2+\beta^2y^2}+\bar{x}}}\right]\right\}$$

The second part of the pressure coefficient defined by equation (B17) is obtained by modifying equation (B68) of NASA CR-2543 by replacing $\frac{ik}{\beta^2}$ by ik in the out-of-phase part of the pressure coefficient. Thus, the second part of the pressure coefficient is given as

$$C_p^2(\bar{x},y,0)=\frac{C_2}{\pi}\left\{\frac{4\bar{v}_1}{\beta\bar{\beta}^2}\left[\tan\Lambda+ik\left(\frac{2\bar{x}\tan\Lambda-(3\tan^2\Lambda+\beta^2)y}{4}\right)\right]\bar{U}_2\right.$$

$$+\frac{4\bar{v}_1}{\bar{\beta}^2}\mathrm{Sgn}(y)\left[1+\frac{ik}{2}\bar{v}_1^2\right]\bar{U}_3$$

$$+ik\frac{y^2}{2}\mathrm{Sgn}(y)\tan\Lambda\left[\frac{2\bar{U}_3\,\bar{v}_1}{\bar{\tau}-\bar{v}_1^2}\right]$$

$$\left.+\frac{y}{\beta}\left[1+ik\left(\bar{x}-\frac{3y\tan\Lambda}{4}\right)\right]\log\left(\frac{\bar{\tau}+\bar{v}_1^2+2\bar{v}_1\bar{U}_2}{\bar{\tau}\;\bar{v}_1^2-2\bar{v}_1\bar{U}_2}\right)\right\} \qquad \text{(B22)}$$

where

$$\bar{x}=\xi-x_{c_s} \qquad y=\eta-y_s$$

$$\bar{v}_1^2=\bar{x}-y\tan\Lambda \qquad \bar{\beta}^2=\beta^2+\tan^2\Lambda$$

$$\bar{\tau}^2=\bar{x}^2+\beta^2y^2 \qquad C_2=\left(\nu-\frac{ikM^2}{\beta}\lambda\right)$$

$$\bar{U}_2^2=\frac{\sqrt{\bar{x}^2+\beta^2y}+\bar{x}}{2} \qquad \nu=i\theta_H k\beta$$

$$\bar{U}_3^2=\frac{\sqrt{\bar{x}^2+\beta^2y}-\bar{x}}{2} \qquad \lambda=\theta_H(1-ik\bar{x}_c)$$

The sum of equations (B21) and (B22) form the complete expression of the pressure coefficient that does not contain any frequency limitations. These expressions must be modified by a suitable modification function such that the boundary conditions are satisfied along the edges of the planform boundary. The modification functions that satisfy these constraints are described in NASA CR-2543.

REFERENCES

1. W. S. Rowe, M. C. Redman, F. E. Ehlers, and J. D. Sebastian, "Prediction of Unsteady Aerodynamic Loadings Caused by Leading Edge and Trailing Edge Control Surface Motions in Subsonic Compressible Flow—Analysis and Results," NASA CR-2543, August 1975.

2. J. R. Petrarca, B. A. Harrison, M. C. Redman, and W. S. Rowe, "Reduction of Computer Usage Costs in Predicting Unsteady Aerodynamic Loadings Caused by Control Surface Motions—Computer Program Description," NASA CR-145354, June 1978.

3. M. Landahl, "Pressure Loading Functions for Oscillating Wings with Control Surfaces," AIAA Journal, Vol. 6, No. 2, February 1968.

4. K. W. Mangler and B. F. R. Spencer, "Some Remarks on Multhopp's Lifting-Surface Theory," Reports and Memoranda No. 2926, August 1952.

5. B. L. Hewitt, "AGARD-CP-80-71 Symposium on Unsteady Aerodynamics for Aeroelastic Analysis of Interfering Surfaces," Part II, pp. 14-1 to 14-18.

6. H. Forsching, H. Triebstein, and J. Wagener, "AGARD-CP-80-71 Symposium on Unsteady Aerodynamics for Aeroelastic Analysis of Interfering Surfaces," Part II, pp. 15-1 to 15-12.

7. B. E. Tinling and J. K. Dickson, "Tests of a Model Horizontal Tail of Aspect Ratio 4.5 in the AMES 12-Foot Pressure Wind Tunnel," NACA RM A9G13, 1949.

8. A. D. Hammond and B. A. Keffer, "The Effect at High Subsonic Speeds of a Flap-Type Aileron on the Chordwise Pressure Distribution Near Mid-Semispan of a Tapered 35° Sweptback Wing of Aspect Ratio 4 Having NACA 65A006 Airfoil Section," NACA RM L53C23, 1953.

9. I. Abel and M. C. Sandford, "Status of Two Studies on Active Control of Aeroelastic Response," NASA TM X-2909, September 1973.

10. A. G. Rainey, C. L. Ruhlin and M. C. Sandford, "Active Control of Aeroelastic Response," AGARD-CP-119, pp. 16-1 to 16-8.

1 Report No.	2. Government Accession No.	3. Recipient's Catalog No
NASA CR-3009		

4. Title and Subtitle	5 Report Date
REDUCTION OF COMPUTER USAGE COSTS IN PREDICTING UNSTEADY AERODYNAMIC LOADINGS CAUSED BY CONTROL SURFACE MOTIONS–ANALYSIS AND RESULTS	March 1979
	6 Performing Organization Code
7. Author(s)	8. Performing Organization Report No
W. S. Rowe, J. D. Sebastian,and J. R. Petrarca	
9. Performing Organization Name and Address	10 Work Unit No
The Boeing Commercial Airplane Company P.O. Box 3707 Seattle, Washington 98124	11 Contract or Grant No NAS1-14122
12. Sponsoring Agency Name and Address	13 Type of Report and Period Covered Contractor Report
National Aeronautics and Space Administration Washington, D. C.	14 Sponsoring Agency Code

15. Supplementary Notes

Langley Technical Monitor: Herbert J. Cunningham

Final Report

16 Abstract

Results of theoretical and numerical investigations conducted to develop economical computing procedures have been applied to an existing computer program (see NASA CR-2543) that predicts unsteady aerodynamic loadings caused by leading and trailing edge control surface motions in subsonic compressible flow. Large reductions in computing costs are achieved by removing the spanwise singularity of the downwash integrand and evaluating its effect separately in closed form. Additional reductions are obtained by modifying the incremental pressure term that accounts for downwash singularities at control surface edges. Accuracy of theoretical predictions of unsteady loading at high reduced frequencies is increased by applying new pressure expressions that exactly satisfy the high frequency boundary conditions of an oscillating control surface. Comparative computer results indicate that the revised procedures provide more accurate predictions of unsteady loadings as well as providing reduction of 50 to 80 percent in computer usage costs. NASA CR-145354 describes the computer program.

17. Key Words (Suggested by Author(s))	18. Distribution Statement
Flutter, Wing-Control-Surface Flutter, Aeroelasticity, Structural Dynamics, Aerodynamics, Unsteady Aerodynamics	Unclassified-Unlimited Subject Category 02

19. Security Classif. (of this report)	20. Security Classif. (of this page)	21. No. of Pages	22 Price*
Unclassified	Unclassified	83	$6.00

*For sale by the National Technical Information Service, Springfield, Virginia 22161

NASA-Langley, 1979